MECHANISMS OF PYRITE OXIDATION TO NON-SLAGGING SPECIES

Final Report

Performance Period
September 1, 1994 – August 31, 1997

Grant DE-FG22-94PC94205

Prepared for

NATIONAL ENERGY TECHNOLOGY LABORATORY
The United States Department Of Energy

Dr. Kamalendu Das, Project Manager
Morgantown, WV 26507-0880

Submitted by

Professor Reginald E. Mitchell

High Temperature Gasdynamics Laboratory
Thermosciences Division

Mechanical Engineering Department
Stanford University
Stanford, California 94305

September 2002

Mechanisms of Pyrite Oxidation to Non-Slagging Species

by
Reginald E. Mitchell and A. E. Jacob Akanetuk

High Temperature Gasdynamics Laboratory
Thermosciences Division
Mechanical Engineering Department
Stanford University
Palo Alto, CA

Executive Summary

A project was undertaken to characterize the oxidation of iron pyrite to the non-slagging species magnetite during pulverized coal combustion. The work was aimed at defining the pyrite transformations responsible for the higher slagging propensity of staged, low-NO_x pulverized coal combustor burners. With such burners, coal is injected into a reducing environment. Consequently, the products of pyrite combustion become shifted from non-depositing, oxidized species such as Fe_3O_4 to highly-depositing, reduced species such as FeO and $Fe_{1-x}S$, where x ranges from 0 to 0.125. The propensity for slagging can be minimized by the judicious redistribution of furnace air to maximize the oxide formation rate. This must be accomplished with minimal degradation of other aspects of boiler performance. To effect this, an understanding of the rate-limiting mechanisms of pyrite oxidation is required.

The overall objectives of this project were to characterize the various mechanisms that control overall pyrite combustion rates and to synthesize the mechanisms into a pyrite combustion model. These objectives were achieved. The model produced has the capability of being incorporated into numerical codes developed to predict phenomena occurring in coal-fired boilers and furnaces. Such comprehensive codes can be used to formulate and test strategies for enhancing pyrite transformation rates that involve the minor adjustment of firing conditions. Ultimately, the benefit of this research project is intended to be an increase in the range of coals compatible with staged, low-NO_x combustor retrofits.

Project activities were aimed at identifying the mechanisms of pyrite combustion and quantifying their effects on the overall oxidation rate in order to formulate a model for pyrite conversion during coal combustion. Chemical and physical processes requiring characterization included pyrite intraparticle kinetics and mass transfer, gas-phase kinetics and mass transfer, and carbon matrix kinetics and mass transfer.

In our efforts, time-resolved phase identifications of extraneous pyrite combustion products were used to determine a pyrite oxidation pathway. Combustion tests indicated that pyrite oxidizes through the following reaction sequence:

$$FeS_2 \rightarrow FeS \rightarrow FeO \rightarrow Fe_3O_4 \rightarrow Fe_2O_3 .$$

Pyrite (FeS_2) is transformed to troilite (FeS), which is oxidized to wusite (FeO). The troilite-to-wusite transformation involves oxidation of an oxysulfide melt $(Fe\text{-}S\text{-}O)_{melt}$ to an iron-oxide melt $(Fe\text{-}O)_{melt}$. Magnetite (Fe_3O_4, really, $FeO \cdot Fe_2O_3$) crystallizes from the oxide melt after complete melt oxidation. At high oxygen levels, crystallized magnetite is oxidized to hematite (Fe_2O_3). Pyrrhotite ($Fe_{1-x}S$) is a product of FeS_2 decomposition that rapidly oxidizes as part of the

oxysulfide melt. Based on the above reaction sequence, a detailed chemical reaction mechanism for pyrite oxidation was developed. The mechanism was employed in models developed for the oxidation of extraneous pyrite particles and pyrite inclusions in coal.

A key feature of the experimental approach taken was the utilization of feed materials characterized by uniformity in size, composition and morphology. The use of feed materials with carefully controlled properties eliminated the uncertainty inherent in using mean values to interpret data obtained with natural materials composed of thousands of individual particles differing in size, composition and morphology.

Scanning electron microscopy, X-ray diffraction spectroscopy, and wavelength dispersive spectroscopy were some of the analytical techniques employed to characterize partially oxidized pyrite samples that were obtained under controlled combustion conditions. Quantitative analyses indicated that intraparticle chemical kinetics controlled the overall oxidation rates of extraneous pyrite particles. Intraparticle gradients in composition were found to be insignificant, indicating that intraparticle mass transport was negligible. Carbon matrix mass transfer and chemical kinetics as well as pyrite intraparticle kinetics control the overall transformation rates of pyrite inclusions in coal. The carbon matrix retards the transport of oxygen to the outer surfaces of included pyrite particles, thereby retarding their rates of oxidation.

With respect to strategies for slag control in staged, low-NO_x pulverized-coal combustor retrofits, the results of this project suggest that pyrite oxidation rates could be accelerated by increasing the heat input to selected burners. This would increase temperatures, thereby increasing the transformation rate of highly adhesive, reduced species such as FeS and FeO to the non-adhesive, oxidized species such as Fe_3O_4 and Fe_2O_3. Since carbon matrix mass transfer and kinetics retard pyrite transformation to magnetite, finer grinding of the coal feed to liberate pyrite inclusions would enhance the rate of the overall pyrite conversion process. In addition, smaller coal-char particles would have higher internal oxygen levels (higher effectiveness factors) and hence, pyrite inclusions would have higher rates of oxidation.

Introduction

This research project fulfills overall efforts to improve our technical understanding of the high-temperature chemical and physical processes involved in the conversion and utilization of coal. The work focuses on the mechanistic description and rate quantification of the effects of fuel properties and combustion environment on iron pyrite transformation to non-slagging species in staged, low-NO_x combustors.

Air staging is an important NO_x reduction technique that has the adverse effect of enhancing slagging problems in boilers that fire pyrite-containing coals. Slagging, the formation of molten deposits on steam tubes by mineral matter, reduces the performance, reliability, and efficiency of power plants. The mineral deposits on the furnace walls impede heat transfer and cause erosion. When deposits accumulate, they may fall and cause mechanical damage.

Among the mineral species most strongly implicated in slagging is iron pyrite (FeS_2) [1]. Pyrite derivatives, known to decrease ash fusion temperatures, are believed to initiate deposition, as iron compounds are commonly observed in the slag layer adjacent to furnace walls [2].

During combustion, pyrite transforms according to the following scheme [3]:

$$FeS_2 \rightarrow Fe_{1-x}S \rightarrow (Fe\text{-}S\text{-}O)_{melt} \rightarrow FeO{\cdot}Fe_2O_3 \rightarrow Fe_2O_3 \, .$$

The iron oxysulfide melt (Fe-S-O) phase of this sequence initiates deposition because of the high deposition efficiency of reduced iron (Fe^{2+}) phases such as $Fe_{1-x}S$ and FeO. These reduced iron compounds lower the melting point and viscosity of the ash particles in which they reside. Air staging as a NO_x reduction technique increases slagging because air staging creates locally reducing zones in the furnace. A reducing environment favors the formation of the reduced iron compounds over the oxidized iron compounds.

One approach to slagging abatement is the prudent adjustment of firing conditions, such as the redistribution of furnace air to form an air curtain for the furnace wall. The aim is to favor the quick formation of non-adhesive oxidized phases such as Fe_3O_4 (*i.e.*, $FeO{\cdot}Fe_2O_3$) over highly adhesive reduced phases such as $Fe_{1-x}S$ and FeO. Any firing condition adjustment would, however, create minimal disturbance on the low-NO_x system.

To meet the stipulation of minimal boiler disturbance by a firing condition adjustment scheme, a fundamental understanding of pyrite combustion is required. If the rate-controlling mechanism of pyrite combustion were identified and quantified, then the optimum boiler conditions could be determined. An identification of the rate-limiting mechanism would suggest exactly which boiler setting to change. Furthermore, a pyrite reaction rate equation could be incorporated into a numerical code, along with NO_x correlations to predict boiler performance after the suggested changes in boiler settings. The firing conditions for obtaining both adequate pyrite oxidation and NO_x reduction could be predicted, for different boilers and coal types. Therefore, there exists an incentive to study the transient evolution of pyrite as a means of motivating control strategies for slagging in staged low-NO_x pulverized-coal combustor retrofits.

Background

As a general introduction to the technological incentive for understanding slagging, the review paper by Reid [1] is helpful. Mineral matter deposition is shown to be a limiting factor on the performance of pulverized-coal power plants. The physical and chemical bases of slagging are covered in a review by Badin [2]. Cited are studies that establish that Fe^{2+} phases such as $Fe_{1-x}S$

and FeO tend to deposit more than Fe^{3+} phases such as Fe_2O_3. These studies are confirmed by Abbott and Austin [4], who demonstrated that FeS has a higher propensity for deposition than Fe_2O_3, thereby arresting earlier speculations that Fe_2O_3 initiates deposition.

Jorgensen [5] investigated the combustion of pure pyrite particles in various size classes at various oxygen levels (from 0% to 21%, by volume), furnace wall temperatures (from 670 to 1170 K), and residence times (from 10 to 210 ms). Qualitative X-ray diffraction analysis, Leco furnace determinations of sulfur content, and atomic adsorption spectroscopic measurements of iron established that at high temperatures, combustion occurs in three stages. First, there is pyrite preheating to an ignition temperature near 870 K at which point desulfurization commences. Second, desulfurization proceeds until complete pyrite conversion to pyrrhotite ($Fe_{1-x}S$) by 970 K; and third, there is formation of a Fe-S-O melt, with rapid escalation of particle temperature to 1750 K as oxidation progresses, forming FeO and Fe_2O_3. Jorgensen found that decreasing particle size, increasing oxygen level and increasing temperature all accelerated the desulfurization rate. The impact of particle size was shown to increase with decreasing oxygen level.

Asaki *et al* [6] monitored the oxidation of pyrrhotite ($Fe_{0.97}S$) and found that particle size becomes important in operating domains with low oxidation rates. Qualitative X-ray diffraction analysis established that pyrrhotite is converted to magnetite ($FeO \cdot Fe_2O_3$) and negligible amounts of Fe_2O_3. Below 825 K, smaller sized pyrite particles (nominally 51 μm) exhibited a significant higher oxidation rate than larger ones (nominally 88 μm). Above 923 K, the oxygen level minimized the significance of both wall temperature and particle size on the conversion rate.

Srinivasachar and Boni [3] developed a model for the combustion of pure pyrite particles, treating the process as being analogous to coal combustion. In their model, pyrite (FeS_2) pyrolyzes to pyrrhotite ($Fe_{0.875}S$), and then oxidizes to Fe-S-O and later to $FeO \cdot Fe_2O_3$. If the oxygen level is high enough and the temperature low enough, the $FeO \cdot Fe_2O_3$ continues to oxidize to form Fe_2O_3. The duration of the oxysulfide melt was found to be sensitive to pyrite particle size, associated carbon, oxygen level, and temperature. Consequently, pyrite-induced slagging is sensitive to these factors.

The work of Akan-Etuk and Niksa [7] and Akan-Etuk [8] provides additional information on the fundamental mechanisms that affect the pyrite transformation rate during combustion. Quantitative X-ray diffraction analysis and scanning electron microscopy revealed that as either the temperature, oxygen level, or residence time was increased, particle morphology shifted from core-and-shell, to round with uniformly dispersed mixed phases, and then to round and totally homogeneous as melting progressed. Even in the same combustion environment, each type of morphology was represented among particles, suggesting that particle size plays a role in establishing the significance of intraparticle processes. The work suggests further that in order to follow the chemical pathway pyrite particles follow during their transformation to magnetite, narrow size distributions are required to get uniform conversion.

Huffman *et al* [9] considered the impact of the carbon associated with the pyrite in coal and found that associated carbon retards pyrite oxidation. Their work suggests an impact of the carbon matrix on pyrite conversion rates, indicating that pyrite intraparticle mass transport resistances becomes relatively less important when the pyrite is encased in carbon.

Project Objectives

Previous studies suggest six mechanisms that have the potential to control the rate of pyrite oxidation to non-slagging species during pulverized coal combustion: pyrite intraparticle kinetics and mass transfer, carbon matrix kinetics and mass transfer, and gas-phase kinetics and mass transfer. Determining the rate-limiting mechanism of pyrite oxidation is an important issue with respect to defining the appropriate operating strategies for the following reasons:

- If pyrite intraparticle kinetics is rate-limiting, then pyrite oxidation could be accelerated by increasing the heat input to selected burners to increase particle temperatures .
- If pyrite intraparticle mass transfer is rate-limiting, then pyrite oxidation could be accelerated by grinding the feed for greater fineness to reduce the pyrite particle size. Also, the heat input could be increased for an enhancement of diffusion through the porous particles.
- If gas-phase kinetics is rate-limiting, then the overall pyrite oxidation rate could be accelerated by increasing the heat input to selected burners to increase the gas temperature or by increasing excess air levels. The intent is to promote sulfur oxidation at the particle surface thereby increasing the driving force for diffusion.
- If gas-phase mass transport is rate-limiting, then the overall reaction rate could be enhanced by accelerating the rate of transport of oxygen to the particle surface via an increase in gas temperature, a decrease in feed particle size, or an increase in turbulence intensity.
- If carbon matrix kinetics is rate-limiting, grinding the feed to liberate pyrite inclusions would enhance the overall pyrite conversion process.
- If carbon matrix mass transfer is rate-limiting, then pyrite oxidation could be accelerated by grinding/classifying the feed for greater fineness to reduce the coal particle size.

In order to determine which effect is rate-limiting at specified operating conditions, it is necessary to investigate the rate of pyrite conversion in such a way that the possible mechanisms can be characterized individually. Obtaining the information needed to characterize the individual mechanisms that control pyrite conversion was an objective of this project. An additional objective was to use the information obtained to formulate an expression to predict the overall rate of pyrite combustion transformation for specified operating conditions.

This final report summarizes the significant results of the project. The experimental procedure is briefly described as are the analytical techniques used to characterize samples of pyrite and its ashes that were produced under controlled oxidation conditions. Conclusions reached about the rate-limiting processes during pyrite transformation to magnetite are presented and discussed. Also presented and discussed is a comprehensive heterogeneous oxidation mechanism capable of describing the formation and destruction rates of the various intermediate species observed in the combustion tests. The mechanism is employed in models put forth for the oxidation of extraneous pyrite particles and for pyrite inclusions in coal. The twelve quarterly reports that were prepared and sent to our U.S.D.O.E. Project Managers (initially, Dr. Margie Kotzalas followed by Dr. Kamalendu Das, Morgantown Energy Technology Center, Morgantown, WV), give details of the work performed, including all calibration procedures. All the data amassed during the course of this project and all data analysis are contained in the Ph.D. thesis of Akanetuk [10]. The calibration procedures, parameters determined for reaction rate coefficients, and validation techniques are also presented in Akanetuk's thesis.

Experimental Approach

Research activities were targeted at providing a fundamental understanding of the combustion conditions that influence the transformation of pyrite to magnetite. To this end, pyrite particles were oxidized under well-controlled conditions. The pyrite conversion process was characterized by examining particles extracted at successive residence times from oxidizing environments.

Batches of homogeneous pyrite particles were utilized in combustion tests, which were performed in an entrained flow reactor designed to simulate environments in typical pulverized coal combustors [11]. The atmospheric pressure laminar flow reactor was fed by an array of diffusion flamelets fueled by CH_4- H_2-O_2-N_2 mixtures that could be adjusted to provide homogeneous post-flame environments having oxygen levels from trace amounts up to 30 mol-% in the temperature range 1100 to 2000 K.

Due to heat losses at the quartz walls of the reactor, the gas temperature drops about 9 K/cm along the reactor centerline where pyrite particles flowed. Gas temperatures were measured using silica-coated thermocouples. Radiation corrections were made to determine the local gas temperature at the thermocouple bead position. Pyrite feed-rates were sufficiently low (about 1 g/hr) so as not to significantly alter the gas composition or temperature profiles established inside the flow reactor.

Samples of pyrite ash were extracted isokinetically from the reactor using a helium-quenched, solids sampling probe [11]. The probe was fixed in position whereas the reactor could be moved vertically, permitting the extraction of particles at selected residence times. The quenched stream of pyrite ash and combustion products was directed to a filter assembly, where the pyrite ash was removed and the gases passed through to a moisture drop-out tube. The dried gas stream was exhausted to the outside atmosphere. In some tests, the pH of the solution in the drop-out tube was measured using Universal pH Indicator Paper. Measured values were in the range 4 - 6. The acidic pH was attributed to sulfuric acid, a byproduct of sulfur oxidation.

The extracted solids were subjected to various analyses for characterization. Particle sizes were measured using a Coulter Multisizer, an instrument based on an electroresistive method for measuring the sizes of small particles. The Multisizer was programmed to classify particles into 256 bin sizes, giving a particle diameter resolution of up to 0.4 μm. The size measurements were confirmed via microscopy.

Apparent and true densities were determined by mercury intrusion porosimetry and helium pycnometry, respectively. Particle morphology was examined by optical and scanning electron microscopy (SEM). Microscopy was also used to judge the significance of intraparticle transport processes. When used in the backscatter mode, a SEM permits the observation of gradients in particle chemical composition. If intraparticle transport processes are fast, then the particles appear to be homogeneous.

X-ray diffraction (XRD) analysis was used to determine the bulk composition of samples employing a technique developed by Akan-Etuk [9] to determine constituent concentrations of iron compounds from analysis of peak locations and peak heights of resulting diffraction patterns. Intrinsic calibration curves were developed using FeS_2 and Fe_3O_4 as reference standards. When evaluated against mixtures of known compositions, the calibration curves were confirmed to be accurate to within 5% relative [8].

Secondary electron and backscatter electron imaging were performed to examine the uniformity in particle morphology and composition. Iron, sulfur and oxygen X-ray maps were generated to characterize element distributions within particles and wavelength dispersive spectroscopy (WDS) was used for quantitative elemental analysis. Calibration curves were developed using Fe_2O_3 and FeS_2 as standards. During WDS analysis, micron-radius hemispherical volumes bisected by sectioning planes were sampled. Energy dispersive spectroscopy (EDS) and Mössbauer spectroscopy were also used to determine the pyrite and pyrrhotite contents of selected solid samples.

The time-resolved data were used to adjust Arrhenius parameters that describe the reaction rate coefficients of reactions in a pyrite oxidation mechanism. Reactions are included that describe the formation and destruction rates of all intermediate species observed in the pyrite oxidation tests. The mechanism permits the calculation of pyrite particle composition and temperature at selected times for specified initial pyrite particle conditions and specified environmental conditions.

Pyrite Preparation

The pyrite utilized in the project was prepared from 60/200 mesh premium grade pyrite, obtained from American Minerals. Nominally, the premium grade pyrite is at least 98% pure, with the impurities being primarily quartz. XRD analysis of pulverized pyrite samples confirmed quartz as being the only significant impurity present in the premium grade pyrite stock. Visual examination by optical microscopy in the transmission mode also confirmed the presence of quartz.

The pyrite stock was pulverized and screened to reduce the mean particle diameter to the 20 μm size range. Size distributions measured using the Coulter Multisizer revealed that the pulverized, screened pyrite stock had a median diameter of 24 μm with geometric standard deviations of σ_{g+} = 1.63 and σ_{g-} = 1.74. [Since the size distribution is not symmetrical about the mean value, two values of the standard deviation are reported: σ_{g+} and σ_{g-}. Assuming a log-normal distribution, about 68% of the particles have diameters between D_v/σ_{g-} and $D_v\ \sigma_{g+}$, where D_v is the median diameter. As σ_{g+} and σ_{g-} each approach one, the sample becomes monodispersed.] Although particles were in the desired size range, the distribution was considered to be too broad to establish definitively the rate-controlling mechanisms. Depending upon oxidation conditions, the larger particles could conceivably have oxidation rates limited by mass transport effects whereas the smaller particles could have oxidation rates limited by chemical kinetic effects. Such differences would complicate data interpretation and could result in erroneous conclusions.

To obtain a narrower size distribution, full sedimentation followed by wet sieving was required. With full sedimentation, oversized particles and any impurity in the pyrite stock having a specific gravity higher than that of pyrite were removed and with wet sieving, particles having diameters smaller than the bottom screen size were eliminated. Measured size distributions indicated that the batch of particles obtained after full sedimentation and wet sieving had a mean size of 19.9 μm with σ_{g+} = 1.205 and σ_{g-} = 1.203, respectively. XRD spectra showed a significant reduction in peaks due to quartz impurities.

Scanning electron microscopy indicated a high degree on uniformity in composition (based on the uniform shading of particles when viewed in backscatter mode). To confirm the apparent interparticle uniformity in composition, selected particles were subjected to energy dispersive spectroscopy (EDS). Several particles were found to be composed exclusively of iron and sulfur, with no impurities.

A secondary electron micrograph (SEM) of the raw pyrite particles used in the combustion tests is shown in Fig. 1. The interparticle variations are not great, as all particles are of the same nominal size, are angular, and are irregularly shaped. The angular morphology constitutes an important reference for assessing the occurrence of melting transformations during combustion.

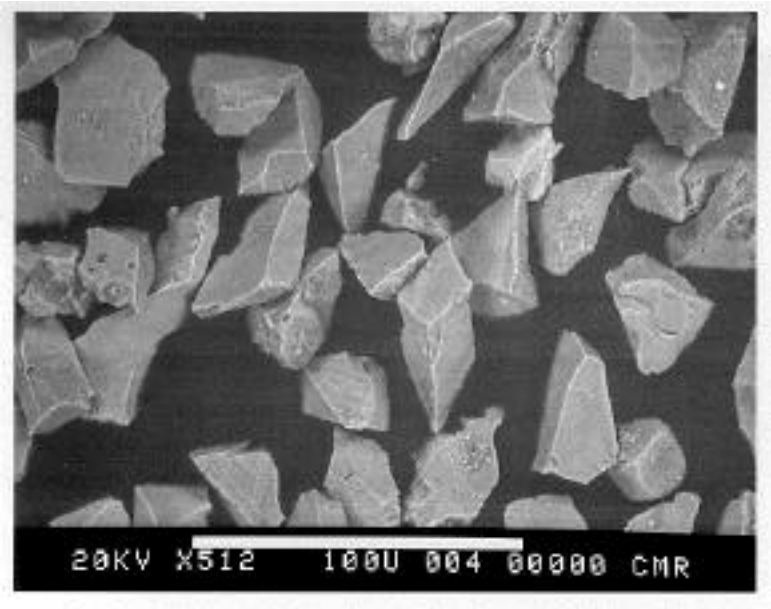

Figure 1. Secondary scanning electron micrograph of raw, unreacted pyrite particles.

A schematic of the laminar flow reactor showing the solids sampling probe positioned along the reactor centerline is shown in Figure 2a and a photograph of pyrite particles oxidizing in the laminar flow reactor is shown in Figure 2b. A pyrite particle heats up and ignites, and becomes engulfed by a luminous yellow flame at a height of approximately 0.65 cm (5 ms) above the reactor inlet plane. The luminous flame results as the sulfur aerosol burns in the boundary layer surrounding the pyrite particle. At 4.4 cm (20 ms), the flame recedes, and the pyrite burns heterogeneously as a glowing orange particle until it is quenched by the sampling probe.

Significant Experimental Results

Combustion tests in 12 mol-% oxygen at 1550 K

Combustion tests were performed to determine the time required for complete oxidation of pyrite under chemical kinetics controlled conditions. To enhance kinetics effects, the temperature in the flow reactor was specified at 1550 K, near the lower end of the industrially relevant temperature range. Higher temperatures would yield pyrite oxidation rates closer to the diffusion-controlled limit, diminishing the impact of chemical kinetics effects. The oxygen concentration was selected to be 12%, by volume. Considerable information has already been obtained on the burning rates of coal chars at these conditions (see for example, Mitchell *et al*. [11,12]). The information on char burning rates can be combined with the results of these experiments to assess carbon matrix effects on pyrite combustion.

Solid samples were extracted from the flow reactor at a residence time of 146 ms, and X-ray diffraction analysis (XRD) was performed on the recovered ash to determine its bulk composition.

When compared with the diffraction pattern of the unreacted pyrite feed, it was noted that almost all the pyrite peaks were transformed to magnetite peaks.

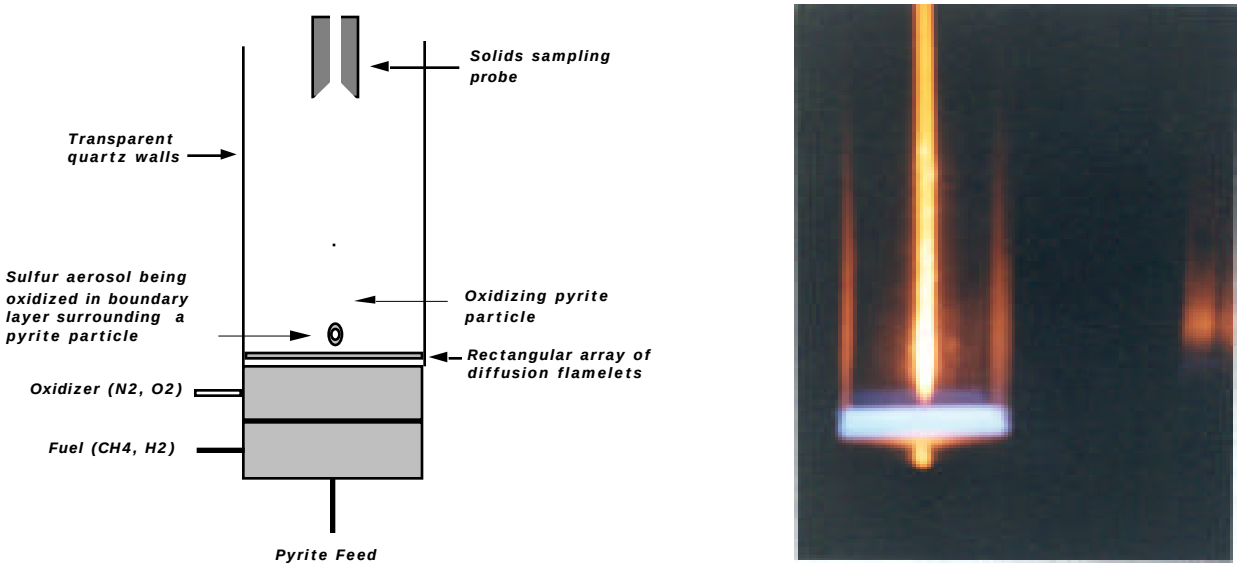

Figure 2. (a) Schematic of the entrained flow reactor showing the sampling probe positioned along the reactor centerline. (b) Photograph of pyrite oxidizing in the flow reactor.

A secondary scanning electron micrograph of particles recovered 146 ms after the onset of oxidation in 12 mol-% oxygen at 1550 K is shown in Fig. 3. The SEM reveals that almost all the particles are spherical, inferring that the pyrite particles had experienced a softening or melting transition. Some of the particles are solid spheres while others are cenospheres or core-and-shells. The particle size varies but most particles have diameters near 20 μm.

The particles were analyzed for elemental variations by energy dispersive spectroscopy (EDS). It was established that iron was the only heavy element constituent in all of the spherical particles. It was also established that there was no appreciable difference between the compositions of the cores and the shells. Non-iron elements, primarily quartz, were found in the non-spherical particles.

Scanning electron micrographs of cross-sectioned particles indicated a high degree of intraparticle uniformity. The external surfaces of particles were found to be rough, not amorphous. Internally, the particles were quite smooth, and they possessed no discernible pore structure. The sectioned particles were of uniform brightness when viewed in backscatter mode, indicative of a lack of atomic number variations.

The size distribution of the recovered ash at the 146-ms residence time was measured with the Coulter Multisizer. Results indicate that oxidation reduces the median size from 19.9 μm to 19.0 μm. Based on mass balance and specific gravity considerations, the calculated size of a pyrite particle having an initial diameter of 19.9 μm is 17 μm after complete conversion to solid magnetite. Evidently, oxidation does not lead to significant fragmentation under the conditions of these tests. The series of oxidation tests in 12 mol-% oxygen indicated that pyrite is fully converted to magnetite after 146 ms of reaction at 1550 K.

Figure 3. Secondary scanning electron micro- graph of pyrite after oxidation for 146 ms in 12 mol-% oxygen at 1550 K.

Solid samples were also extracted from the flow reactor at residence times of 22, 25, 36 and 109 ms in the 12 mol-% oxygen environment at 1550 K. Approximately 90% of the particles extracted after 22 ms of oxidation were angular and on the order 20 μm in diameter. These partially oxidized particles were similar to the feed material, except that the oxidized pyrite particles exhibited greater micro-roughness.

Some spherical particles were present and some of the angular particles had 10 μm-spherical particles attached. The spherical particles exhibited crystallites in varying degrees, and were deemed to be either pure magnetite or magnetite-pyrite mixtures .

The X-ray diffraction pattern of the angular particles contained no peaks that could be attributed to a pyrrhotite intermediate ($Fe_{1-x}S$). Data analysis indicated that the sample contained roughly 82% pyrite (FeS_2) and 18% magnetite ($FeO \cdot Fe_2O_3$). The absence of pyrrhotite is consistent with Jorgensen's observation that the formation of trace amounts of magnetite precedes the formation of pyrrhotite [5]. This suggests that the troilite-to-wusite and the wusite-to-magnetite transformation steps were extremely rapid in the 12 mol-% oxygen environment at 1550 K.

Only wusite (FeO) and magnetite were observed on the XRD patterns of ash particles recovered after 25 ms of reaction. Scanning electron micrographs revealed that almost all the particles were spherical and on the order of 20 μm. A few particles appeared to be segregated into pairs of 10 μm particles. Crystallites were quite apparent in most particles. The ash composition was estimated to be 11 wt-% wusite and 89 wt-% magnetite.

The 22-ms residence time test suggests that the $FeS_2 \rightarrow FeS$ transition is rate-limiting in 12 mol-% oxygen at 1550 K, since only pyrite and magnetite were observed. The 25 ms test suggests that the $FeO \rightarrow Fe_3O_4$ transition becomes rate-limiting 3 ms later, as FeO was the only magnetite precursor observed.

The ash captured and characterized via XRD after 36 ms of reaction in 12 mol-% oxygen at 1550 K contained only wusite and magnetite. The composition was established to be 7 wt-% wusite and 93 wt-% magnetite. A micrograph revealed that about 95% of the particles were perfect spheres. Several particles appeared to be undergoing a self-segregation (or sintering) transformation. Practically all particles exhibited crystallites.

Approximately 90% to 95% of the particles extracted after 109 ms of oxidation were observed to be spherical, the remainder being angular. The angular particles tended to be somewhat larger than the spherical ones. Only magnetite peaks were discernible on a X-ray diffraction pattern of the 109-ms ash particles.

Combustion tests in 1 mol-% oxygen at 1550 K

Combustion tests were performed in flow reactor environments containing 1 mol-% oxygen at nominally 1550 K. At the low oxygen concentration, oxidation rates are slower than in 12 mol-% oxygen, making it easier to identify intermediate oxidation pathways. In these tests, ash was recovered at times of 42, 52, 77, and 146 ms after pyrite injection. X-ray diffraction (XRD) analysis was used to determine the bulk composition of the recovered ash. Secondary electron and backscatter electron imaging were performed to examine the uniformity in particle morphology and composition. Iron, sulfur, and oxygen X-ray maps were generated to characterize element distributions within particles, and wavelength dispersive spectroscopy (WDS) was used for quantitative elemental analysis.

42-ms Test

A scanning electron micrograph (SEM) of particles extracted 42 ms after pyrite injection into the 1 mol-% O_2 environment is shown in Fig. 4. Almost all the particles are angular and on the order of 20 μm. A few particles show evidence of softening, indicative of transformations of pyrite (FeS_2) to troilite (FeS). The diameters of those particles that have presumably undergone a melting or softening transformation are approximately 15 μm. The micrograph confirms that prior to oxide formation, pyrite experiences a softening transformation.

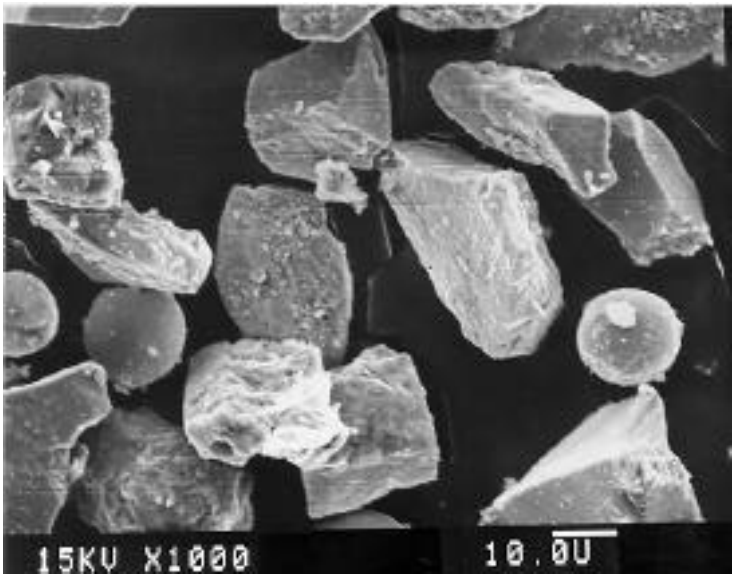

Figure 4. Secondary electron micrograph of pyrite particles after 42 ms of oxidation in 1 mol-% O_2 at 1550 K.

Figure 5 shows the diffraction pattern resulting from X-ray diffraction analysis of sectioned particles. Peaks due to pyrite, troilite, and pyrrhotite 3T (non-stoichiometric pyrrhotite, $Fe_{0.875}S$) are identified. The broadening of the troilite peak is indicative of a softening transition.

The bulk composition determined using the intrinsic XRD calibration curves developed during the course of this project indicate that particles are primarily pure FeS_2 with small quantities of $Fe_{0.875}S$ and nearly stoichiometric FeS. The composition was estimated to be 90 wt-% pyrite, 6 wt-% non-stoichiometric pyrrhotite and 4 wt-% troilite. Thus, the onset of pyrite oxidation is attributed to be either of the following reactions: $FeS_2 \rightarrow FeS$ or $FeS_2 \rightarrow Fe_{0.875}S$.

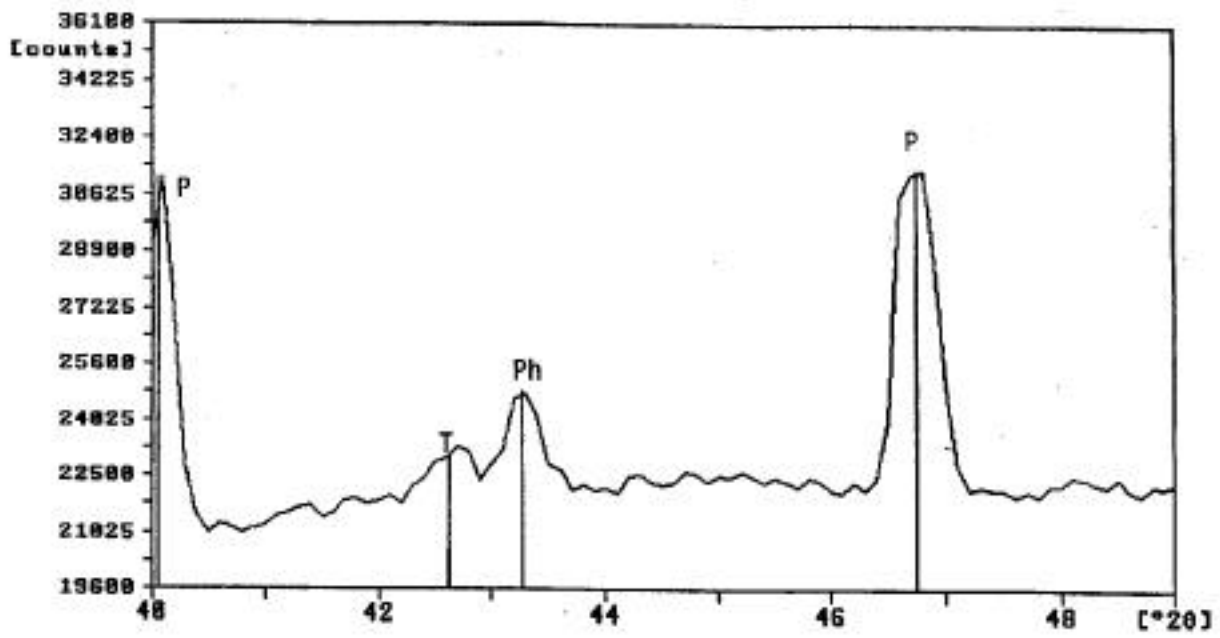

Figure 5.X-ray diffraction pattern of pyrite after oxidation at 1550 K in 1 mol-% oxygen for 42 ms. Present are peaks due to pyrite (P), pyrrhotite 3T (Ph), and troilite (T)

Many backscatter-imaged SEMs were obtained of particles extracted at 42 ms residence time. The images were optimized for contrast since brightness correlates with weight-averaged atomic number. Shown in Fig. 6 is a typical backscatter-imaged SEM of sectioned particles. Labeled are the points on which quantitative WDS elemental analyses were performed. From the brightness, it may be inferred that spherical particles possess a greater averaged atomic number than angular ones. While there are internal pockets of low brightness, noticeable shading within particles is restricted to particle edges (a common artifact of SEMs), and different luminosity zones are mixed in a non-organized fashion. In effect, gradients in intraparticle brightness on the scale of the particle radius are not significant.

Results of quantitative WDS analyses are shown in Table 1. Shown are normalized atomic ratios of iron, sulfur, and oxygen for sampling positions numbered in Fig. 6. These measurements indicate that angular particles are FeS_2 and spherical particles are $Fe_{0.80}SO_{0.24}$ (omitting the low-

weight total point 7, $FeS_{0.82}O_{0.24}$). The measurements establish that intraparticle variations in atomic ratio are less than ±5% (except particle 6's and 7's oxygen ratio, which is ±15%).

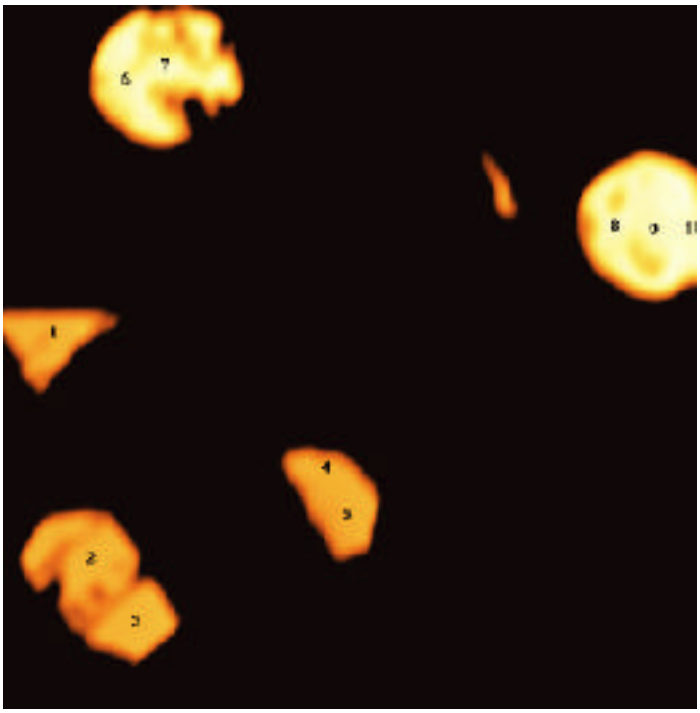

Figure 6. Backscatter scanning electron micrograph of particles after reaction for 42 ms in 1 mol-% O_2 at 1550 K.

Table 1.
WDS Analyses of Pyrite after Reaction at 1550 K and 1% Oxygen for 42 ms

Position	Fe	S	O
1	1.000	2.054	0.004
2	1.000	2.016	0.000
3	1.000	2.034	0.000
4	1.000	2.004	0.000
5	1.000	1.992	0.000
6	1.000	0.773	0.286
7*	1.000	0.727	0.212
8	1.000	0.828	0.237
9	1.000	0.827	0.229
10	1.000	0.842	0.216

* Low weight total, 91.58%

Element X-ray maps are shown in Fig. 7. An iron X-ray map is presented in Fig. 7a. Particle shapes are different from those in Fig. 6 since X-rays originate from a greater depth than do backscatter electrons. Spherical particles, due to their higher volumetric concentrations of iron atoms, appear brighter than angular particles. Intraparticle gradients in intensity are perceptible only in the particles in the upper right corner (next to particle 8 of Fig. 6), however. The image is degraded because the particle lies deep within the epoxy. Therefore, the dullness of the left side may be due to the particle's comprising two attached particles. In general, the iron appears well dispersed within particles.

An atomic sulfur distribution map is shown in Fig. 7b. In this image, angular particles are brighter than spherical ones, in contrast with the iron map of Fig. 7a. The only significantly non-uniform particle is the angular one in the upper-right corner. As in Fig. 7a, the left side of this particle is somewhat darker than the right side. Again, intraparticle uniformity in intensity is evident in most particles.

Presented in Fig. 7c is an oxygen map, and the map indicates that there is significantly more oxygen in the epoxy than in the particles. Although angular particles are completely dark, the spherical particles exhibit evidence that they contain a minor amount of oxygen. [The oxygen may be due to adsorption or vacancy occupation.] Consistently anomalous, the left side of the particle

in the upper-right corner of the picture contains even greater oxygen than the epoxy. With the exception of this particle, intraparticle gradients in composition are not noticeable.

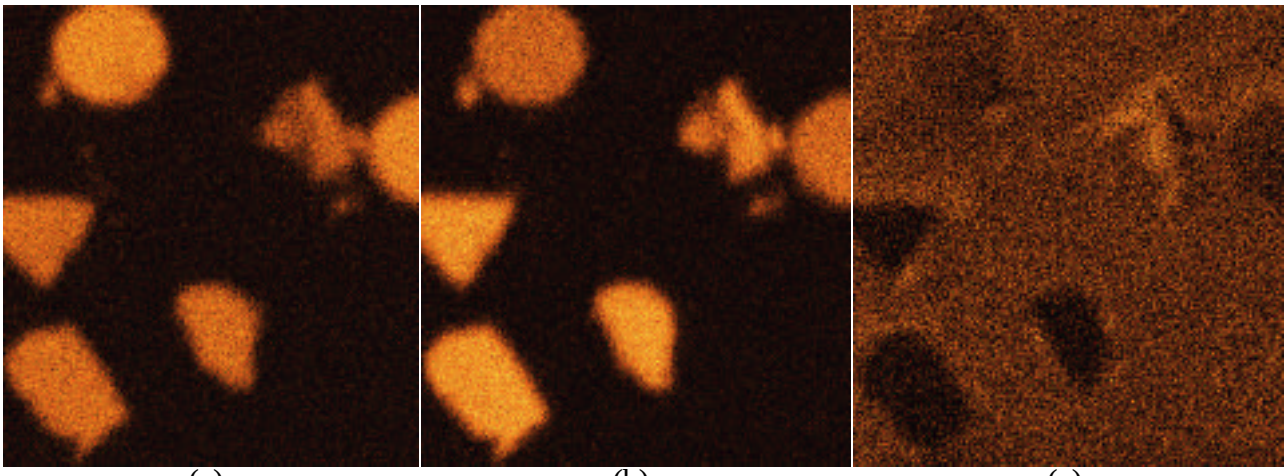

(a) (b) (c)

Figure 7. (a) Iron, (b) sulfur, and (c) oxygen X-ray maps of particles after reaction for 42 ms in 1 mol-% O_2 at 1550 K.

Other WDS data also suggest a high degree of intraparticle mixedness. Shown in Table 2 are WDS analyses for non-angular particles (angular particles are always FeS_2), some of which are contained in the SEM of Fig 8. Among the non-angular particles, even particle-to-particle variations are small. In general, the particles can be characterized as $FeS_{0.98}O_{0.12}$. Variations in sulfur ratio and oxygen ratio are ±1.5% and ±12.6%, respectively.

Table 2.
WDS Analyses of Pyrite after Reaction at 1550 K and 1% Oxygen for 42 ms

Particle	Fe	S	O
Semi-Plastic (5)	1.000	0.966	0.138
Nodule (4)	1.000	0.995	0.107
Crescent (6)	1.000	0.842	0.240
Mesosphere	1.000	0.971	0.112
Sphere	1.000	0.986	0.137

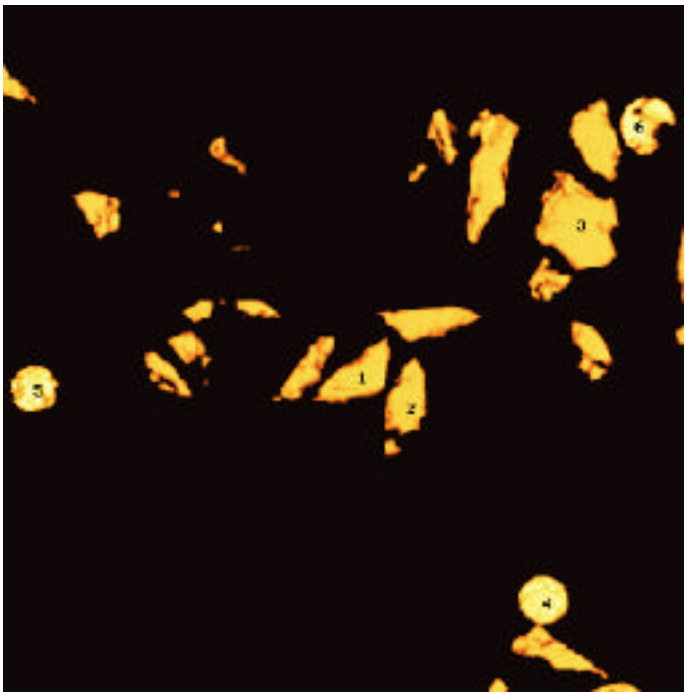

Figure 8. Backscatter scanning electron micrograph of particles after reaction for 42 ms in 1 mol-% O_2 at 1550 K.

52-ms Test

A scanning electron micrograph (SEM) of particles extracted 52 ms after pyrite injection into the 1 mol-% O_2 environment at nominally 1550 K is shown in Fig. 9. A variety of particle shapes exist, indicating that interparticle variation in composition is greater after 52 ms of reaction than at 42 ms. Present are angular, spherical, and highly irregular particles of approximately 20 μm in size. There are also a few spherical particles having diameters as small as 5 μm.

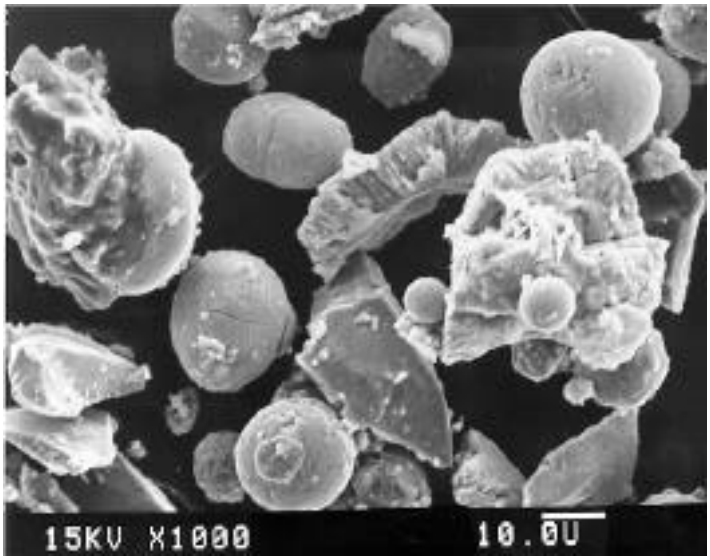

Figure 9.Secondary electron micrograph of pyrite particles after 52 ms of oxidation in 1 mol-% O_2 at 1550 K.

An XRD pattern of the recovered ash after 52 ms of reaction is shown in Fig. 10. The iron oxide peak is only slightly shifted from that of perfectly-stoichiometric wusite, FeO. Almost completely absent is the pyrrhotite 3T peak observed at 42 ms residence time. The troilite peak is approximately two times its previous width, suggesting that additional softening has occurred. The relative concentrations assigned to the species using the calibration curve developed are 39 wt-% pyrite, 53 wt-% troilite, and 8 wt-% wusite. The appearance of wusite suggests that the second step in the oxidation pathway is FeS → FeO.

Despite the particle-to-particle variations, intraparticle differences in composition are relatively minor. Backscatter SEMs of sectioned particles and the elemental X-ray maps suggest that radius-scale intraparticle gradients in composition are not substantial after 52 ms of reaction. Shown in Fig. 11 is one of several backscatter SEMs of sectioned particles. Angular and semi-plastic particles are duller than round particles. Within particles, dark spots due to focusing effects and macrovoids are evident. The SEM suggests that intraparticle gradients in composition are modest inside particles.

Many WDS measurements were made, and Table 2 contains the WDS results for the points shown in Fig. 11. For those particles with only one WDS sampling point, intraparticle uniformity can be inferred by using WDS data in conjunction with backscatter SEMs and X-ray maps. The interparticle variations in composition are greater than that observed after 42 ms of reaction. There are now particles of lower sulfur and correspondingly high oxygen levels. There is even a FeS_2 particle with excess sulfur (or iron deficit): point 6. It should be noted that the weight total for this particle, 95.04%, is significantly lower than that of the next worst FeS_2 particle, 97.08%.

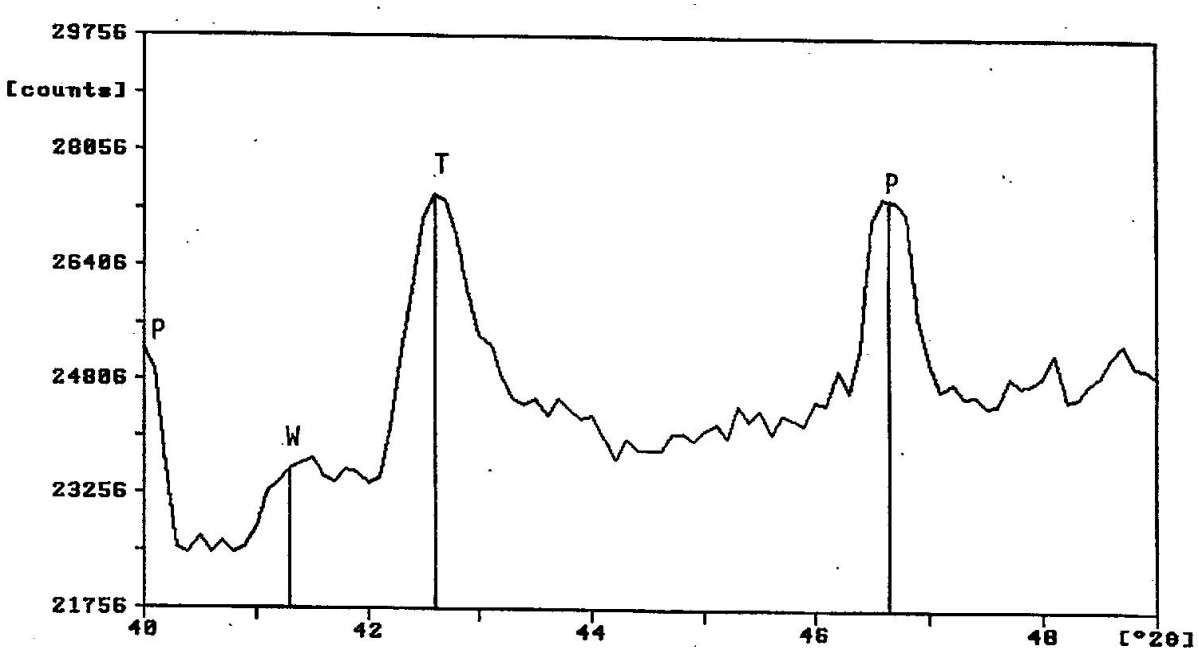

Figure 10. X-ray diffraction pattern of pyrite after oxidation at 1550 K in 1 mol-% oxygen for 52 ms. Present are peaks due to pyrite (P), troilite (T), and wusite (W).

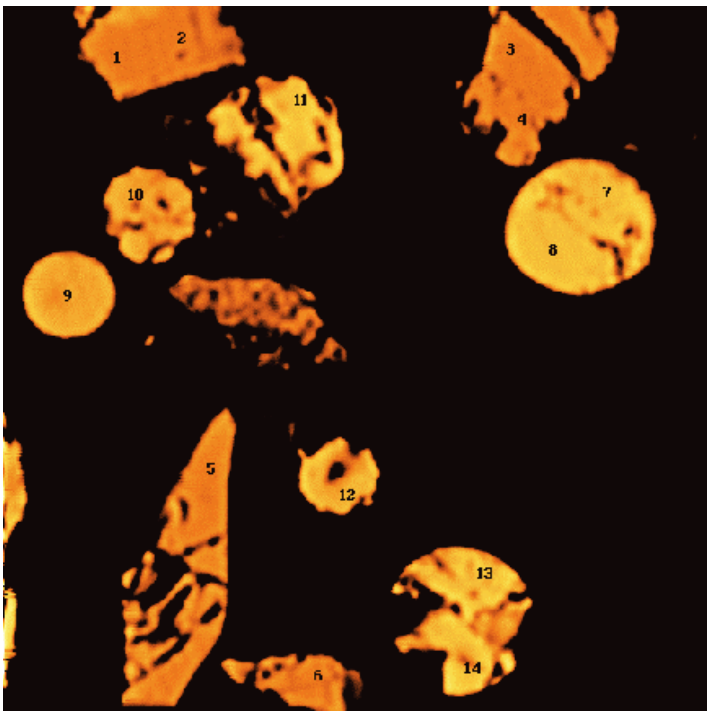

Figure 11. Backscatter scanning electron micrograph of 20-μm diameter pyrite particles after reaction for 52 ms in 1 mol-% O_2 at 1550 K.

Table 2.
WDS Analyses of Pyrite after Reaction at 1550 K and 1% Oxygen for 52 ms

Position	Fe	S	O
1	1.000	2.013	0.004
2	1.000	2.032	0.018
3	1.000	2.016	0.000
4	1.000	2.020	0.019
5	1.000	2.023	0.000
6	1.000	2.126	0.028
7	1.000	0.825	0.241
8	1.000	0.813	0.221
9	1.000	0.363	0.734
10*	1.000	0.285	0.823
11	1.000	0.691	0.389
12**	1.000	0.541	0.908
13***	1.000	0.834	0.316
14	1.000	0.801	0.288

* Low weight total, 94.42%
** Low weight total, 94.60%
*** Low weight total, 92.44%

Elemental iron, sulfur and oxygen X-ray maps are shown in Fig. 12. The iron X-ray map of the particles is presented in Fig. 12a. There is slightly greater iron concentration in the spherical particles than in the angular and semi-plastic particles. Within the resolution of the map, there do not appear to be significant radius-scale intraparticle gradients in iron content.

The sulfur X-ray map (Fig. 12b) indicates that there exists an interparticle variation in sulfur content. The angular and semi-plastic particles have a high sulfur content. The spherical particles range from intermediate to low brightness. The particles of low brightness appear spotty, perhaps indicative of mixture of sulfur-containing and non-sulfurous grains. Other than edge effects, radius-scale intraparticle gradients in sulfur content are not detectable.

The oxygen X-ray map (Fig. 12c) contains particles that exhibit substantially greater oxygen content than the epoxy background. Angular particles (points 1, 2, 3, 4, 5, and 6 in Fig. 11) are oxygen deficient. Semi-plastic particles show a deficit (points 3 and 4) as well as high oxygen level (point 11). Generally, high oxygen level is associated with spherical particles (points 9, 10, and 12), but there is a hollow shell next to point 7 (barely visible in Fig. 11) that also exhibits high oxygen level. Although angular particles are uniformly low in oxygen content, the intraparticle dispersion of oxygen in non-angular particles is difficult to discern.

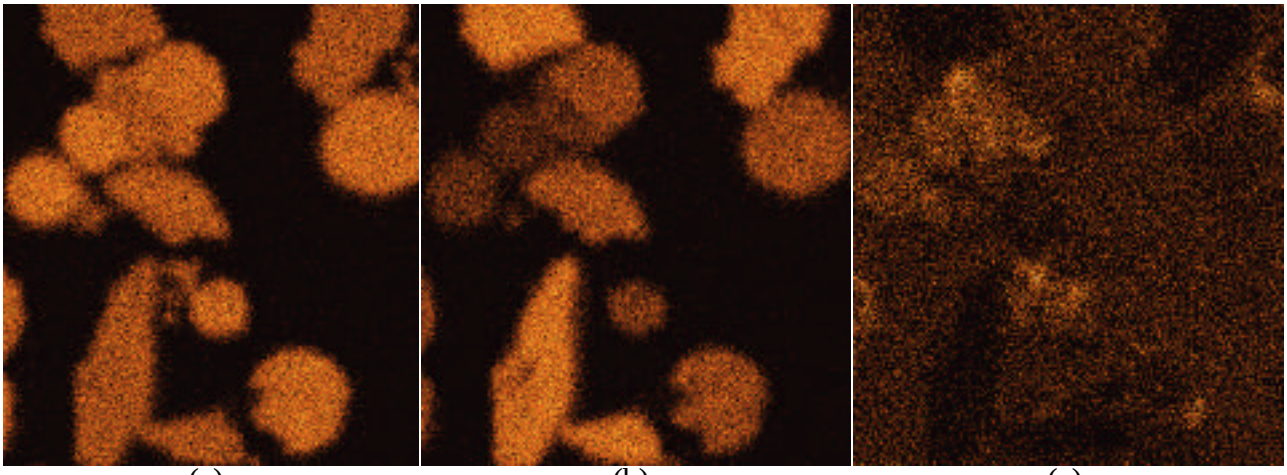

(a) (b) (c)

Figure 12. (a) Iron, (b) sulfur, and (c) oxygen X-ray maps of particles after reaction for 52 ms in 1 mol-% O_2 at 1550 K.

77-ms Test

A scanning electron micrograph of pyrite particles that have reacted in 1 mol-% O_2 at 1550 K for 77 ms is shown in Fig. 13. Although almost all of the particles are spherical, there are still noticeable interparticle variations. Some of the objects that contribute to the heterogeneity in the micrograph are actually pieces of the cracked shells of spherical particles. Some particles exhibit 5 μm craters on their surfaces that sometimes contain spherical nodules. In most particles, the crystallites are evident.

An X-ray diffraction pattern of a sample of the ash recovered after 77 ms of reaction is displayed in Fig. 14. The diffraction pattern shows peaks due to troilite, and wusite. The width of the wusite

peak remains essentially unchanged from its width at 52 ms but the troilite peak width is decreased from its earlier value.

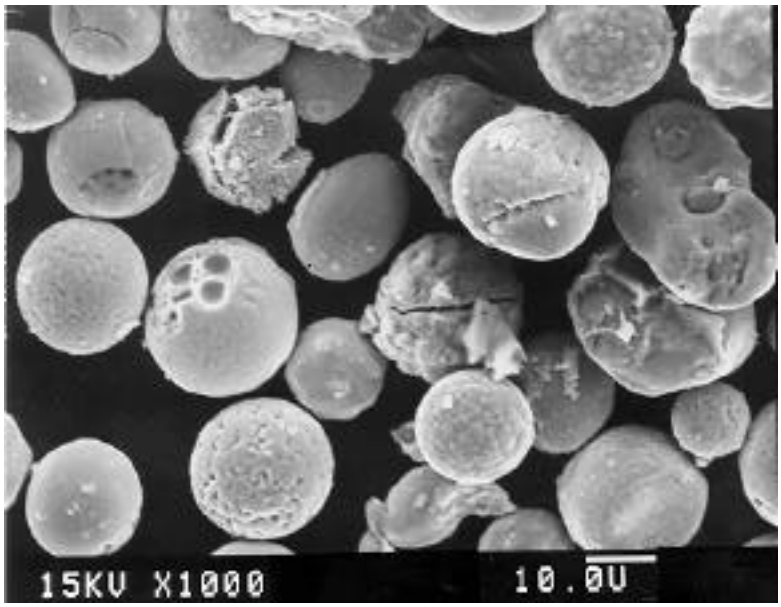

Figure 13. Secondary electron micrograph of pyrite particles after oxidation in 1 mol-% O_2 at 1550 K for 77 ms.

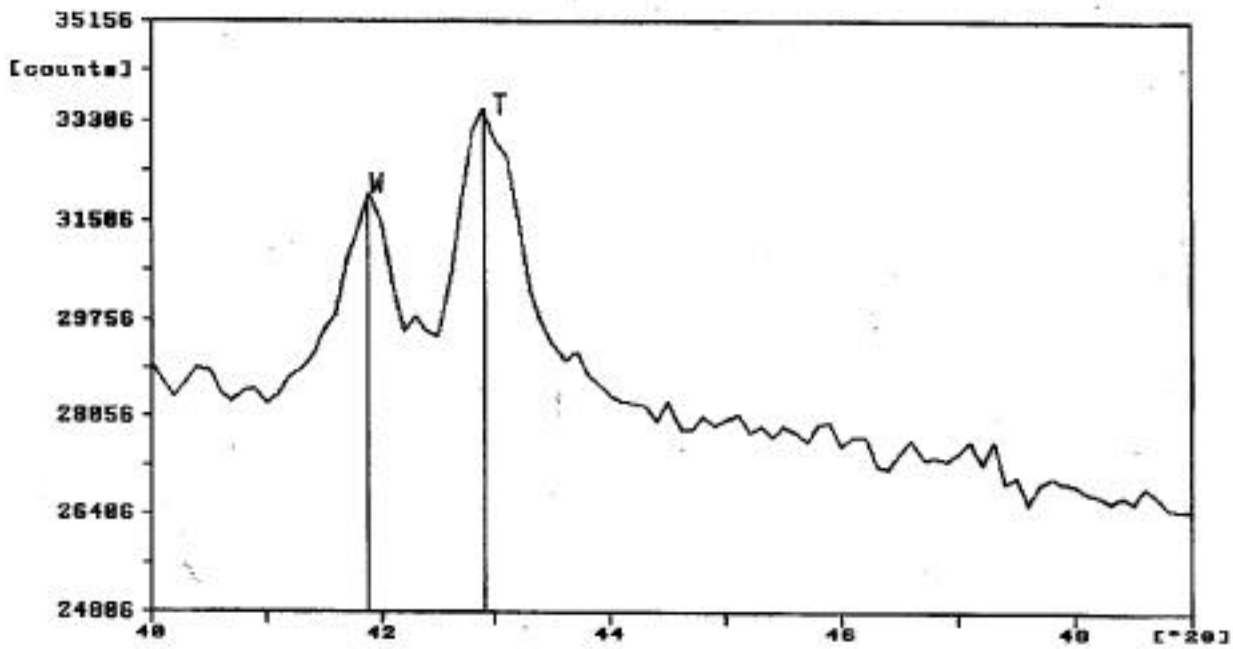

Figure 14. X-ray diffraction pattern of pyrite after oxidation at 1550 K in 1 mol-% oxygen for 77 ms. Present are peaks due to troilite (T) and wusite (W). Pyrite is also present at this reaction time.

The observation of wusite and troilite at this reaction time reinforces the previous inference that the second step of pyrite oxidation is FeS → FeO. Furthermore, the absence of pyrrhotite 3T in this test and the 52 ms test is consistent with the view that FeS_2 → FeS is a more significant decomposition mechanism than FeS_2 → $Fe_{0.875}S$. Based on the intrinsic calibration curves, the composition of the condensed phase after 77 ms of reaction in 1 mol-% oxygen at 1550 K is approximately 26 wt-% pyrite, 30 wt-% troilite, and 44 wt-% wusite.

A backscatter scanning electron micrograph of a sample of the material collected at the 77 ms-residence time is shown in Fig. 15. The SEM contains primarily spherical and crescent particles. Semi-plastic particles and cenospheres are also present.

The micrograph suggests the existence of multiple phases within particles. Dark (low atomic number) finger-like patches are interspersed in a bright matrix. Edge effects (dark patches) are prominent in the brightest particles. Generally, the radius-scale intraparticle structure shows no preference of radial position as the dark, finger-like patches grow. Consequently, this SEM is interpreted as implying that particles become well mixed internally as more of the lower atomic number phase is formed.

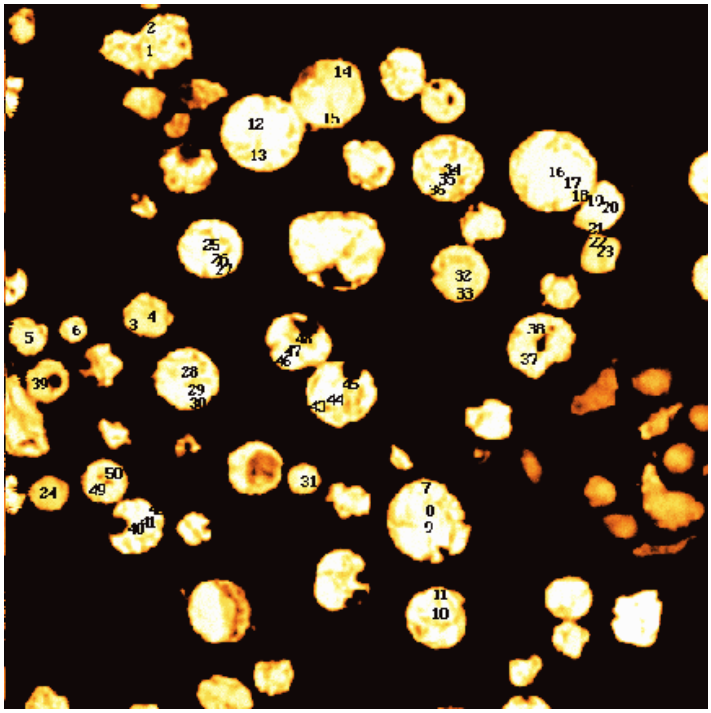

Figure 15. Backscatter scanning electron micrograph of 20-μm diameter pyrite particles after reaction for 77 ms in 1 mol-% O_2 at 1550 K.

Tabulated in Table 3 are elemental compositions for points labeled in Fig. 15. The variation in sulfur atomic ratio ranges from ±0.5% to ±5%, except for points 3 and 4. For these points, the variation is as high as ±36%. Oxygen variations typically range from ±0.2% to ±13%. For three particles, the variation is 22%, 32% and 33%. The WDS measurements establish that intraparticle variations in composition are somewhat larger at 77 ms than at earlier times.

146-ms Test

A scanning electron micrograph of pyrite particles that have reacted in 1 mol-% O_2 at 1550 K for 146 ms is shown in Fig. 16. Although over 80% of the particles are spherical, there are noticeable interparticle variations. Evident are angular, unreacted pyrite particles, as the pyrite was fired as a dense suspension for a portion of the tests duration. Pieces of cracked shells of spherical particles also add to the interparticle variations. The crystallites in the particles are quite noticeable.

Table 3. WDS Analysis of Pyrite after Reaction at 1550 K and 1 mol-% Oxygen for 77 ms (see Fig. 15 for sampling positions)

Position	Fe	S	O	Weight Total*(%)	Position	Fe	S	O	Weight Total*(%)
1	1.000	1.004	0.101		26	1.000	0.804	0.290	
2	1.000	0.982	0.200		27	1.000	0.806	0.299	
3	1.000	0.154	1.050		28	1.000	0.578	0.601	
4	1.000	0.072	1.190	93.53	29	1.000	0.553	0.578	93.96
5	1.000	0.290	0.934		30	1.000	0.543	0.495	94.99
6	1.000	0.359	0.875		31	1.000	0.788	0.378	
7	1.000	0.772	0.313		32	1.000	0.254	0.934	
8	1.000	0.807	0.357		33	1.000	0.232	0.880	
9	1.000	0.778	0.322		34	1.000	0.988	0.092	
10	1.000	0.908	0.155		35	1.000	0.994	0.079	
11	1.000	0.931	0.161	94.90	36	1.000	0.945	0.154	94.62
12	1.000	0.864	0.203		37	1.000	0.696	0.461	
13	1.000	0.850	0.173	94.79	38	1.000	0.704	0.463	
14	1.000	0.722	0.673		39	1.000	0.001	1.287	
15	1.000	0.696	0.515		40	1.000	0.714	0.356	
16	1.000	0.570	0.591		41	1.000	0.728	0.386	
17	1.000	0.568	0.575		42	1.000	0.746	0.417	
18	1.000	0.548	0.570		43	1.000	0.878	0.182	
19	1.000	0.726	0.550		44	1.000	0.870	0.181	
20	1.000	0.733	0.435		45	1.000	0.869	0.235	
21	1.000	0.775	0.687		46	1.000	0.769	0.296	
22	1.000	0.117	1.066		47	1.000	0.760	0.307	
23	1.000	0.124	0.944	94.68	48	1.000	0.823	0.385	93.04
24	1.000	0.131	1.150	93.70	49	1.000	0.376	0.756	
25	1.000	0.794	0.334		50	1.000	0.365	0.821	

*Only weight totals below 95% are shown

An X-ray diffraction pattern of the ash recovered 146 ms after the onset of oxidation in 1 mol-% oxygen at 1550 K is presented in Fig. 17. The XRD analyses of particles detected primarily Fe_3O_4 and nearly stoichiometric FeO. Unreacted pyrite was also detected due to the dense pyrite suspension that was fired (inadvertently) during portions of the test. The approximate composition of the ash (pyrite-free) was established to be 14 wt-% wusite and 86 wt-% magnetite. This 146-ms test establishes that the final step in pyrite oxidation leads to the formation of magnetite through the transition $FeO \rightarrow Fe_3O_4$.

Sectioned oxidized particles revealed that the particles were more mixed internally than those at 77 ms. One of the backscatter SEMs obtained for sectioned particles is presented in Fig. 18. [The

dark spherical regions are cavities in the epoxy.] Generally, the particles appear more mixed internally than those at 77 ms after reaction, although dark, finger-like patches are still discernible.

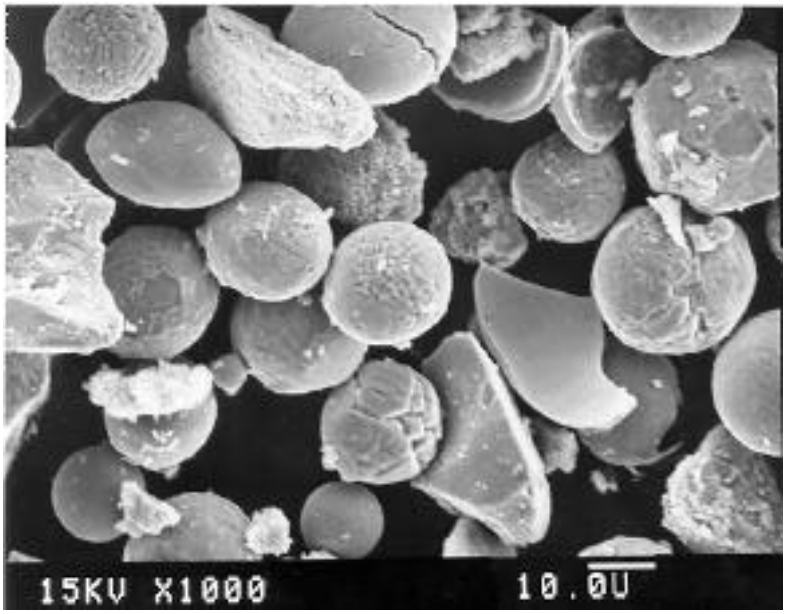

Figure 16. Secondary electron micrograph of pyrite particles after oxidation in 1 mol-% O_2 at 1550 K for 146 ms. Unreacted pyrite (angular particles) are present due to the dense suspension fired during the test.

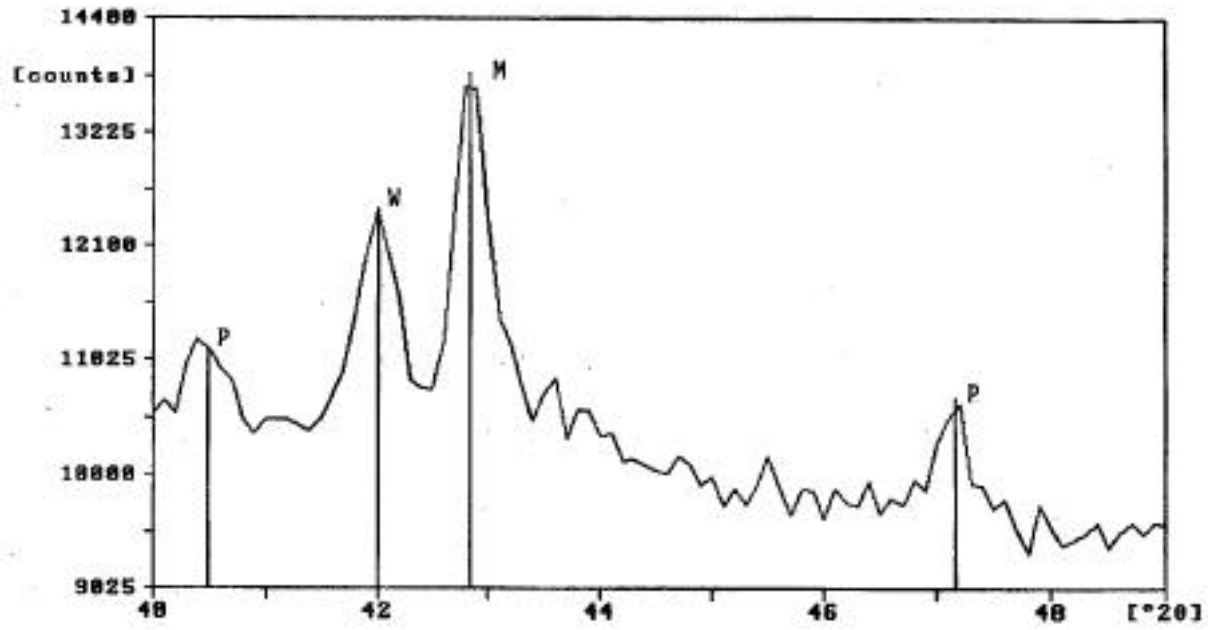

Figure 17. X-ray diffraction pattern of pyrite after oxidation of a dense suspension of pyrite at 1550 K in 1 mol-% O_2 for 146 ms. Present are peaks due to wusite (W), magnetite (M), and unreacted pyrite (P).

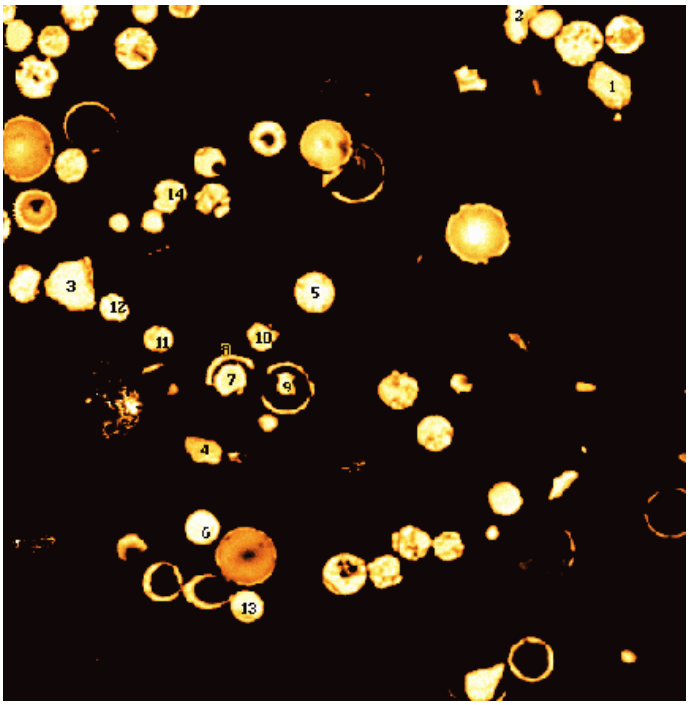

Figure 18. Backscatter scanning electron micrograph of 20-μm diameter pyrite particles after reaction for 146 ms in 1 mol-% O_2 at 1550 K.

Table 4. WDS Analyses of Pyrite after Reaction at 1550 K in 1% Oxygen for 146 ms

Position	Fe	S	O
5	1.000	0.265	0.898
6	1.000	0.076	1.038
7	1.000	0.001	1.197
8	1.000	0.002	1.170
9	1.000	0.016	1.358
10	1.000	0.002	1.307
11	1.000	0.064	1.291
12	1.000	0.164	0.932
13	1.000	0.220	0.974
14	1.000	0.001	0.385
14 (again)	1.000	0.001	0.319

Shown in Fig. 19 are elemental X-ray maps that were obtained for particles in the triangular region formed by points 4, 5, and 11 in Fig. 18. The iron X-ray map indicates that despite interparticle differences, within each particle there are no radial gradients in iron content. Spherical particles have higher iron contents than other particles. Within the same particle, however, even cores and shells exhibit the same intensity. It should be noted that spherical particles exhibit patches that correspond to different grain types.

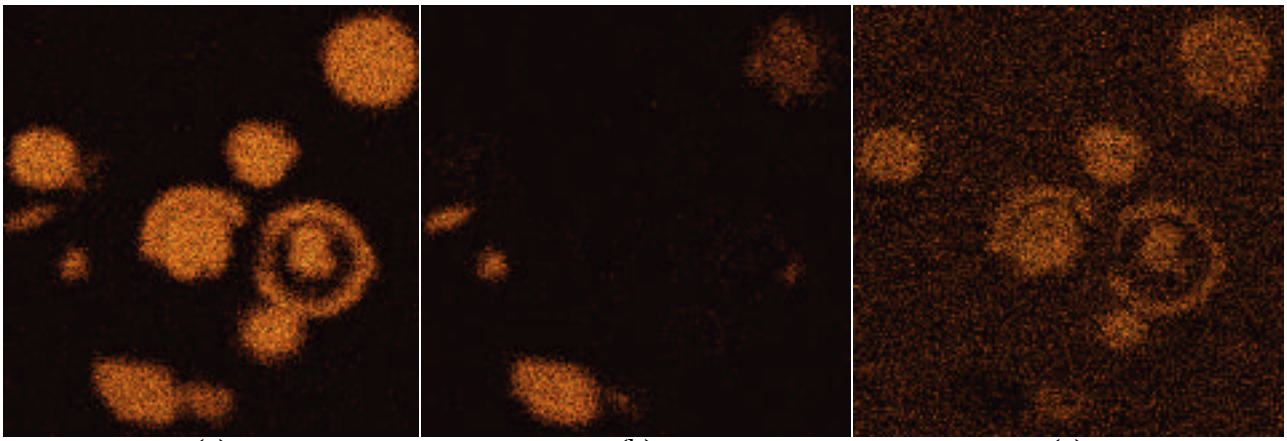

(a) (b) (c)

Figure 19. (a) Iron, (b) sulfur, and (c) oxygen X-ray maps of particles after reaction for 146 ms in 1 mol-% O_2 at 1550 K.

The sulfur X-ray map indicates that although interparticle variations are prominent, there is adequate mixing within each particle, on the scale of the particle radius. Angular particles and

some spherical particles have noticeable levels of sulfur, but spherical core-and-shells and some spherical particles are devoid of sulfur. At point 5, sulfur is associated with a dentritic structure emanating from the particle center. Nevertheless, on the scale of the particle radius, the particle may be considered thoroughly mixed.

The oxygen X-ray map at the 146 ms reaction time suggests that intraparticle mixing is thorough. Again, radius-scale intraparticle gradients appear negligible.

Discussion

Chemical Kinetics-Controlled Oxidation

Calculations indicate that in the entrained flow reactor tests, pyrite oxidation occurred at a rate significantly lower than the external diffusion-limited rate based upon the average gas temperature. This suggest that intraparticle chemical kinetics processes are rate-limiting for most stages of oxysulfide oxidation of 20 μm pyrite particles at 1550 K average gas temperature.

Quantitative characterizations of pyrite oxidation in 1 mol-% oxygen at 1550 K inferred that at 42 ms, the reaction FeS → FeO was rate-limiting, based on the observation that FeS was building up with no substantial FeO or Fe_3O_4 detected. By 52 ms (and for the remainder of the characterized residence times), the reaction FeO → Fe_3O_4 had become rate-limiting, as FeO was building up without significant Fe_3O_4 until FeS_2 and FeS had been depleted. For at least the last 64% of particle life in 1 mol-% O_2 at 1550 K, FeO → Fe_3O_4 was rate-limiting.

In 12 mol-% oxygen at 1550 K, quantitative characterizations revealed that at 22 ms of reaction time, the reaction FeS_2 → FeS was rate-limiting (Fe_3O_4 was building up with no substantial FeS or FeO detected). By 25 ms, the reaction FeO → Fe_3O_4 had become rate-limiting, (as FeO had built up while FeS_2 and FeS had become depleted).

Detailed analyses of the WDS measurements of pyrite samples from all four residence times of the 1 mol-% oxygen tests revealed that particle compositions were either pure FeS_2 or blends of O and S with Fe. Based on the S/Fe and O/Fe ratios, five major combinations of iron compounds were identified [10]: 1) FeS-O* blend: FeS_xO_y regions, where $1.021 > x > 0.995$ and $0.070 < y < 0.107$. Initially, atoms of O are incorporated into FeS, but insufficiently for a distinct phase to emerge. The * symbol denotes that a species is present but has not formed a distinct phase. When an alloying element is added to a given metal, a sufficient amount of the solute has to be incorporated into a structure before a distinct phase emerges [13]. 2) FeS-O*-Fe* blend: FeS_xO_y regions, where $1.021 > x > 0.727$ and $0.070 < y < 0.286$. For these particles, atoms of O have been substituted for S, but insufficiently incorporated into a structure for FeO to emerge. 3) FeS-FeO-O*-Fe* blend: FeS_xO_y regions, where $0.726 > x > 0.265$ and $0.288 < y < 0.898$. By this point, enough O atoms had replaced S atoms to form a distinct FeO phase. 4) FeO-O*-Fe*-S* blend: FeS_xO_y regions, where $0.254 > x > 0.072$ and $0.934 < y < 1.190$. After the majority of S atoms had been replaced, FeS disappeared as a distinct phase, FeO became the dominant compound, and supersaturated O sites formed. 5) FeO-Fe_3O_4-O*-Fe*-S*: FeS_xO_y regions, where $0.072 > x > 0.001$ and $1.190 < y < 1.358$. Continued oxidation of the oxysulfide formed a distinct Fe_3O_4 phase, and S/Fe atomic ratio decreased to the 0.001 level. The demarcations of the last three phase combinations are blurred.

The raw microprobe and SEM analyses of oxidized pyrite revealed that in general, particles could be modeled as being well stirred, having negligible compositional gradients of the scale of the

particle radius. To further examine issues related to radial gradients, single particle multiple measurements were examined using the Thiele modulus framework as well as regression analysis [10]. The S, Fe, and O concentrations were cast in terms of atom percents, without normalization with respect to Fe. The concentrations were tabulated according to the particle and radial position from which they were obtained. Radial positions, r, were defined for the sectioned particles as either 0 for the center, 0.5 for the midway point between the center and the edge, or 1.0 for the edge. For each particle, a correlation coefficient was calculated between the radial position and the concentration of each element. A positive correlation meant that concentration increased radially outward. At the same time, an average composition was calculated, based on a simple average of the particle's radial profile. The average was used in conjunction with the composition at r = 1.0 to calculate the effectiveness factor.

The analysis of radial gradients confirmed that generally each element's radial gradients were small and without preferred orientation. Generally, the effectiveness factors of each element were approximately equal to 1.0, indicative of uniform concentration. The typical ranges of effectiveness factors were 0.99 - 1.02, 0.99 - 1.03, and 0.97 - 1.04 for Fe, S, and O respectively. The effectiveness factors for S possessed two outliers, one at a particle for which $\eta = 0.73$ and the other at a particle for which $\eta = 0.75$. These particles had low S/Fe levels (values of 0.154 and 0.072 at the particle for which $\eta = 0.73$ (at points 3 and 4 of Fig. 15) and values of 0.001 and 0.002 at the particle for which $\eta = 0.75$ (at points 7 and 8 of Fig. 18)). The effectiveness factors for O contained more outliers, including particles for which $\eta = 0.71$ and 0.76. These particles had S/Fe levels near 1.0 and low O/Fe levels (values of 0.092, 0.079 and 0.154 at the particle for which $\eta = 0.71$ (at points 34, 35, and 36 of Fig. 15), and values of 0.101 and 0.200 at the particle for which $\eta = 0.76$ (at points 1 and 2 of Fig. 15)). Two mesospheres also had somewhat low O effectiveness factors ($\eta = 0.90$ and 0.93) when moving from particle center to macrovoid, whereas they had effectiveness factors of approximately 1.0 when moving from particle center to particle surface. On the other hand, another mesosphere of slightly lower S/Fe and greater O/Fe possessed an effectiveness factor roughly equal to 1.0 in both directions. In short, the early stage of FeS oxidation approached FeS core-and-O shell transformation, whereas the late stage of Fe_3O_4 formation approached Fe_3O_4 core-and-S shell transformation.

Low values of the effectiveness factor suggest that the oxysulfide stages of pyrite combustion are kinetically limited. The only definite exception was the beginning of the oxidation process, during which transport effects were important. At that point, the O/Fe atomic ratio was ~0.15. In addition, certain points in the middle of the Fe_3O_4 formation stage were conceivably transport-limited, as the S atoms in two samples exhibited low effectiveness factors. It should be noted, however, that the S/Fe atomic ratio was very low, in the range 0.001 - 0.154, and the noise level for S/Fe readings was 0.001. Furthermore, it was not obvious that the presence of S at that point affected Fe_3O_4 formation rate or particle properties.

The correlation coefficients of concentration versus radial position are equally likely to be positive or negative. Iron had a negative correlation in 60% of the cases, meaning that typically Fe concentration decreased radially outwards. The positive Fe radial correlation coefficients were concentrated in particles of compositions $S/Fe < 0.6$ with $O/Fe > 0.6$, *i.e.*, FeO-containing particles. Sulfur had an almost equal number of positive radial correlations as negative radial correlations, but the negative correlations were concentrated in particles of compositions $0.8 > S/Fe > 0.1$ with $0.7 < O/Fe < 1.0$. These were particles of FeO with small amounts of FeS. Oxygen had a positive radial correlation coefficient in 56% of the cases, and the negative

correlation coefficients were concentrated in particles of S/Fe < 0.6 and O/Fe > 0.6. In other words, in FeO-containing particles, O concentration decreased radially outward. For all three elements, it must be emphasized that these correlation coefficients rarely corresponded to steep concentration gradients.

Correlation of the radial concentration profiles of Fe, S, and O with each other was determined [10], and the results indicated that Fe atom-% and O atom-% were almost always negatively correlated. Sulfur versus O exhibited negative correlations in almost 70% of the cases and Fe and S were positively correlated in 60% of the cases. Basically, Fe and S were negatively correlated whenever S and O were positively correlated, and S and O tended to be positively correlated in the region 0.9 > S/Fe > 0.7 and 0.15 < O/Fe < 0.4. This corresponds to the transformation stage in which O is replacing S, but insufficiently for a distinct FeO phase to emerge.

Pyrite Transformation to Magnetite

Regression analysis of WDS-derived O/Fe atomic ratio versus S/Fe atomic ratio of oxysulfide particles [10] yielded regression line slopes that suggested that after an initial thermal decomposition to form $Fe_{0.875}S$ (*i.e.*, $FeS_2 \rightarrow Fe_{0.875}S$), pyrite transforms according to the following scheme:

$$FeS_2 \rightarrow FeS \qquad \text{(R.a)}$$
$$FeS \rightarrow FeO \qquad \text{(R.b)}$$
$$FeO \rightarrow Fe_3O_4. \qquad \text{(R.c)}$$

The $FeS_2 \rightarrow Fe_{0.875}S$ transition was deduced to be a momentary ignition step that is quickly replaced by reaction R.a as the primary pyrite decomposition step. The regressions also suggested that small amounts of $Fe_{0.875}S$ oxidize to form $Fe_{1-x}O$.

In the 12 mol-% oxygen environment, reactions R.b and R.c were sufficiently rapid that no intermediates were detected until 25 ms. After 25 ms, the reaction products consisted of varying quantities of FeO and Fe_3O_4. Based on the data obtained in the 12 mol-% oxygen environment, at reaction times less than 22 ms, $k_c > k_b > k_a$, where k_k is the reaction rate coefficient for reaction R.k. Hence, reaction R.a was rate-limiting at the onset of pyrite oxidation. Three milliseconds later, reaction R.c had become rate-limiting since only FeO and Fe_3O_4 were detected. The observed change in the rate-limiting reaction is hypothesized to be due to the differing activation energies of the three transformation steps. As oxidation proceeded in the entrained flow reactor tests, the temperatures of the pyrite particles increased, reaching a level to maintain quasi steady-state oxidation rates during the later stages of conversion. Early in the particle history as the particle was heating up, the lowest activation energy reaction was most rapid. At the highest temperature, the lowest activation energy transformation step became least rapid. In other words, the activation energies of the above reactions are in the order $E_c < E_b < E_a$, where E_k is the activation energy of reaction R.k. This ordering of activation energies is consistent with the pyrite oxidation data obtained in the 1 mol-% oxygen tests performed in the entrained flow reactor as well as with data obtained in tests performed in a radiant flow reactor [8].

No direct single particle measurements of Fe, S, and O can be found in the open literature, as required to conclusively establish the relationship between S-atom removal and O-atom addition. In this work, oxygen atoms were evident early within particles of S/Fe atomic ratio of 1.0. The O atoms were dispersed throughout each particle, and this was both before and after completion of the softening transformation. This observation supports the conclusion that during pyrite

decomposition, oxygen reacts with unreacted FeS_2 and that the FeS formation rate may be kinetically-limited. The observation is, however, inconsistent with most studies in the open literature in their assertion that if at all O atoms become thoroughly dispersed within an early stage particle, it is only after particle fusion.

WDS measurements revealed the presence of O atoms even before bulk sample XRD detected FeO, and the WDS measurements also uncovered S atoms even after XRD suggested that FeS had disappeared. Least squares fit of the WDS data [10] suggest that even stoichiometric FeS had $O_{0.126}$ associated with it and stoichiometric FeO had $S_{0.136}$ associated with it. Estimates are that FeO emerged at O/Fe atomic ratio of about 0.28 and FeS disappeared at S/Fe atomic ratio of approximately 0.25. This observation is consistent with the established fact that when an alloying element is added to a given metal, a sufficient amount of the solute has to be incorporated into a structure before a distinct phase emerges [13]. This phenomenon has not been reported for iron pyrite undergoing combustion transformations.

Quantitative characterizations of reaction product composition suggested that the oxygen level of the gas environment affected the pyrite transformation rate throughout particle life. As part of the analysis of oxygen dependency, reaction product compositions were cast in terms of the distribution of total Fe atoms among different iron compounds (FeS_2, FeS, FeO, and Fe_3O_4). At each residence time that ash particles were recovered from the flow reactor, the percentage of the total Fe atoms present in each of the species was obtained for both the 1 mol-% and 12 mol-% oxygen environments. The change of these Fe-atom percentages with time constituted the definition of transformation rates.

For the overall reaction converting pyrite (FeS_2) to magnetite (Fe_3O_4), the global transformation rate was noted to rise more rapidly than the oxygen concentration. In 1 mol-% oxygen, between 42 ms and 146 ms, Fe-as-FeS_2 dropped from 88% to 0% while Fe-as-Fe_3O_4 rose from 0% to 85%. This implied that in 104 ms, 73% of the Fe atoms had shuttled from FeS_2 to Fe_3O_4, yielding a transformation rate of 0.7 Fe%/ms. In 12 mol-% oxygen, 62% of the Fe atoms had undergone the same transformation in 3 ms, yielding a rate of 21 Fe%/ms. While the oxygen level had increased by only a factor of 12, the overall pyrite conversion rate had increased by a factor of 29.

The Pyrite Oxidation Model

Oxidation Mechanism

One limitation of the pyrite oxidation pathway derived from the entrained flow reactor tests was that each step only specified the resulting iron compound during the transformation of the existing iron compound, not the full set of product species. An accurate description of the chemical reaction responsible for the transformation of a particular iron compound would have required determinations of gas-phase primary reaction products. While substantial amounts of sulfur aerosols were recovered during studies performed in the entrained flow reactor as well as previously in the radiant reactor [8], the yields were not sufficiently characterized for accurate determination of reaction product stoichiometries.

Direct determinations of gas-phase reaction products of high temperature pyrite oxidation have not been published. Despite the limited reaction product information for the individual steps of the transformation pathway, a pyrite oxidation mechanism can be proposed based on the results of this

investigation, Huffman *et al.*'s thermodynamics modeling [9], and published pyrite kinetics models. Huffman *et al.* [9] presented the following set of global reactions for pyrite oxidation:

$$\begin{aligned} FeS_2 &\rightarrow FeS + 1/2\ S_2 \\ FeS + 3/2\ O_2 &\rightarrow FeO + SO_2 \\ 3FeO + 1/2\ O_2 &\rightarrow Fe_3O_4 \end{aligned}$$

The first reaction was modified to capture the observed oxygen-independent decomposition of pyrite to pyrrhotite and to reflect the fact that oxygen was noted to accelerate pyrite decomposition. The gas phase product of the second reaction was changed from SO_2 to SO, in keeping with the observations of Jorgensen [5], and the oxygen stoichiometric coefficient in the third reaction was changed to maintain integral units for each species. A comprehensive heterogeneous reaction mechanism for pyrite oxidation that accounts for the salient observations reported is the following:

$$\begin{aligned} FeS_2 &\rightarrow (1\text{-}x)\ Fe_{1-x}S + (1+x)\ S && \text{(R.1)} \\ Fe_{1-x}S + (1+x/2)\ O_2 &\rightarrow (1\text{-}x)\ FeO + SO && \text{(R.2)} \\ Fe_{1-x}S + (1\text{-}x)\ SO &\rightarrow (1\text{-}x)\ FeO + (1\text{-}x/2)\ S_2 && \text{(R.3)} \\ Fe_{1-x}S + (1\text{-}x)\ O &\rightarrow (1\text{-}x)\ FeO + S && \text{(R.4)} \\ FeS_2 + O_2 &\rightarrow FeS + SO_2 && \text{(R.5)} \\ FeS_2 + SO &\rightarrow FeS + S_2 + O && \text{(R.6)} \\ FeS_2 + O &\rightarrow FeS + SO && \text{(R.7)} \\ FeS + O_2 &\rightarrow FeO + SO && \text{(R.8)} \\ FeS + SO &\rightarrow FeO + S_2 && \text{(R.9)} \\ FeS + O &\rightarrow FeO + S && \text{(R.10)} \\ 2FeO + O_2 &\rightarrow Fe_2O_3 + O && \text{(R.11)} \\ FeO + Fe_2O_3 &\rightarrow Fe_3O_4 && \text{(R.12)} \end{aligned}$$

Consistent with observations, it can be assumed that after an initial transient period, the pyrrhotite concentration reaches a quasi steady-state level, which requires that reaction R.1 is slower than either reactions R.2, R3 or R.4, *i.e.*, FeS_2 decomposition is rate-limiting. Pyrrhotite levels would only be appreciable at early times, and the pyrrhotite concentration would decrease with increasing oxygen level. Reactions of pyrite, pyrrhotite and troilite with SO are responsible for elemental sulfur release. Elemental sulfur release is greatest early in the oxidation process, during the formation and destruction of pyrrhotite.

It can also be assumed that the troilite concentration reaches a quasi steady-state level. For this, the slowest of reactions R.8, R.9 and R.10 must be faster than the fastest of reactions R.5, R.6 and R.7, the rate-controlling troilite formation reaction.

The law of mass action is used to relate the rate of change of the concentration of each species A_i to the reaction rate RR_k of each reaction k.

$$\frac{d[A_i]}{dt} = \sum_k \left\{ \left(\nu'_{ik} - \nu_{ik} \right) RR_k \right\}. \qquad (1)$$

In this equation, ν_{ik} is the stoichiometric coefficient of species A_i on the reactants side of reaction R.k, as written above, and ν'_{ik} is the stoichiometric coefficient of species A_i on the products side of reaction R.k, Also, $[A_i]$ denotes the concentration of species A_i in units of [mol/(m^3-fluid)·s] for a

gas-phase species and in units of [mol/(m^2-surface)·s] for a condensed species. The condensed species are the iron-containing species: FeS_2, $Fe_{0.875}S$, FeS, FeO, Fe_2O_3, and Fe_3O_4, and the gas-phase species are S, S_2, SO, SO_2, O, and O_2. Numerical integration of the set of mass action equations yields the concentrations of the various species at selected times.

Reaction rate coefficients (and other pyrite particle properties) must be evaluated at the temperature of the pyrite particle. To determine the temperature of an extraneous pyrite particle, the particle energy balance is employed, wherein the energy generated at the particle surface due to chemical reaction is balanced by energy loss from the particle due to convection and radiation to the surroundings. The unsteady energy balance equation is

$$\rho_p V_p c_{p,p} \frac{dT_p}{dt} = A_p h\left(T_\infty - T_p\right) + A_p \sigma \varepsilon_p \left(T_w^4 - T_p^4\right) + \rho_p V_p S_{g,p} \sum_k \left\{\left(-\Delta h_{rxn,k}\right) RR_k\right\} , \qquad (2)$$

where $c_{p,p}$ is the specific heat of the pyrite particle of external area A_p, volume V_p, and specific surface area $S_{g,p}$; h is the heat transfer coefficient ($h \equiv Nu\ \lambda/d$, where Nu is the Nusselt number and λ is the thermal conductivity of the gas); RR_k is the rate of reaction R.k; and $\Delta h_{rxn,k}$ is the heat of reaction of reaction R.k. The emissivity of the pyrite particle is ε_p and σ is the Stefan-Boltzmann constant. The temperatures of the pyrite particle, the gas, and the walls to which particles radiate are denoted by T_p, T_∞, and T_w, respectively. The specific heat of the particle depends upon the particle's composition.

The law of mass action expression for oxygen yields the following relation for the rate of oxygen consumption ($\dot{O}_2$, in mol-O_2/m^2·s) due to reactions with iron containing species:

$$\dot{O}_2 \equiv -\frac{d[O_2]}{dt} = \left\{k_2[Fe_{0.875}S] + k_5[FeS_2] + k_8[FeS] + k_{11}[FeO]^2\right\}[O_2] . \qquad (3)$$

The overall sulfur release rate ($\dot{S}$, in mol-S/m^2·s) is given by

$$\dot{S} = \frac{d[S]}{dt} + \frac{d[SO]}{dt} + \frac{d[S_2]}{dt} + \frac{d[SO_2]}{dt} =$$

$$= k_1[FeS_2] + \left\{k_2[Fe_{0.875}S] + k_5[FeS_2] + k_8[FeS]\right\}[O_2] + \qquad (4)$$

$$\left\{k_4[Fe_{0.875}S] + k_7[FeS_2] + k_{10}[FeS]\right\}[O] .$$

This equation gives the rate that sulfur would be released to the gas phase if chemistry alone controlled the pyrite oxidation rate. Quasi steady-state assumptions for the $Fe_{0.875}S$ and FeS concentrations would allow this rate to be written in terms of the O_2, O and FeS_2 concentrations. The result would indicate that the sulfur release rate increases as the oxygen concentration of the surroundings is increased and decreases as pyrite is consumed during the oxidation process.

Oxygen Mass Transport to Particles

Extraneous pyrite particles

It is assumed that no reaction occurs in the boundary layers surrounding pyrite particles. This is a valid assumption for particles less than 50 μm. The elemental sulfur and SO are oxidized in the surrounding gas, away from the surfaces of pyrite particles. Oxygen diffuses from the

surrounding gas to the outer surface of the pyrite particle of diameter d_p. The oxygen flux at the outer surface of the pyrite particle, J_{O2} (mol-O_2/m^2·s), is given by

$$J_{O_2} = \frac{Sh\ D_{O_2}}{d_p}\left([O_2]_\infty - [O_2]_s\right) \tag{5}$$

In the above equations, Sh is the Sherwood number and D_{O2} is the effective bulk diffusion coefficient of oxygen through the other gases that compose the surroundings. The equation indicates that the smaller the particle size, the greater the oxygen flux to the particle surface and hence, the higher the desulfurization rate. This is in accord with the observations of Jorgensen [5].

All the oxygen that reaches the outer surface of the pyrite particle is consumed via reaction. Thus, the oxygen flux at the outer surface of the pyrite particle and the oxygen consumption rate due to reaction are related by

$$\pi d_p^2 J_{O_2} = S_{g,p}\rho_p\left(\pi d_p^3/6\right)\dot{O}_2 \quad \text{or} \qquad J_{O_2} = \left(S_{g,p}\rho_p d_p/6\right)\dot{O}_2 \tag{6}$$

where $S_{g,p}$ is the specific surface area of pyrite (m^2/g) and ρ_p is the apparent density of a pyrite particle (g/m^3).

The absence of intraparticle radial gradients in oxygen suggests that $\dot{O}_2$ should be evaluated at $[O_2]_s$. By doing so, Eqs. (3), (5) and (6) can be combined to yield the following expression for the rate of change in the oxygen concentration, assumed to be uniform inside the pyrite particle at the value at the outer surface:

$$\frac{d[O_2]_s}{dt} = \frac{\left(6\ Sh\ D_{O_2}\right)/\left(S_{g,p}\ \rho_p\ d_p^2\right)}{1+\left(6\ Sh\ D_{O_2}\right)/\left(S_{g,p}\ \rho_p\ d_p^2\ f\right)}[O_2]_\infty \tag{7a}$$

where

$$f = k_2[Fe_{0.875}S] + k_5[FeS_2] + k_8[FeS] + k_{11}[FeO]^2\ . \tag{7b}$$

Equations (7a) reveals that the oxygen consumption rate is controlled by the rate of oxygen diffusion to the outer surface of the pyrite particle when $f >> (6\ Sh\ D_{O2})/(S_{g,p}\rho_p d_p^{\,2})$ (*e.g.*, at high temperatures), and controlled by chemical reaction rates when $f << (6\ Sh\ D_{O2})/(S_{g,p}\rho_p d_p^{\,2})$. At any time, the oxygen concentration at the outer surface of the pyrite particle and that in the surroundings satisfies the following relation:

$$[O_2]_s = \frac{\left(6\ ShD_{O_2}\right)/\left(S_{g,p}\ \rho_p\ d_p^2\right)}{\left(6\ Sh\ D_{O_2}\right)/\left(S_{g,p}\ \rho_p\ d_p^2\right)+f}[O_2]_\infty\ . \tag{7c}$$

This equation reveals that the oxygen concentration at the outer surface of the pyrite particle approaches that in the surrounding gas as the rates of chemical reactions decrease (*e.g.*, as temperature decreases).

Equations (1) (for all species except oxygen), (2) and (7a) represent a set of differential equations that must be integrated numerically to yield values of the composition and temperature of an oxidizing extraneous pyrite particle at selected times after the onset of oxidation. Properties of the

surroundings ($[O_2]_\infty$ and T_∞) and particle (d_p, ρ_p, and $S_{g,p}$) must be specified as well as Arrhenius parameters that describe the reaction rate coefficients.

Pyrite inclusions in coal-char

Oxygen diffuses from the surrounding gas to the outer surface of the coal-char particle of diameter d_c. It then diffuses through the pores of the particle, reacting with the pore walls in the process. Under typical conditions that exist in pulverized coal-fired boilers and furnaces, the overall burning rates of the char particles are controlled by the combined effects of pore diffusion and the chemical reactivity of the carbonaceous particle material. Assuming that the porous coal char particles are spherical and isothermal, overall particle burning rates per unit external surface area (q_c, in gC/(m^2-surface)·s) can be expressed as follows [14]:

$$q_c = \left(1 + \frac{\eta \rho_c S_{g,c} d_c}{6}\right) R_{iC,s} \ . \tag{8}$$

Here η is the effectiveness factor of the char particle and $R_{iC,s}$ is the intrinsic chemical reactivity of the char evaluated at the temperature and oxygen concentration at the outer surface of the char particle of apparent density ρ_c and specific surface area $S_{g,c}$. The effectiveness factor accounts for the fact that the oxygen concentration inside the char particle is not uniform. The O_2-concentration is greatest at the outer surface of the particle and decreases as the particle center is approached. For effectiveness factors near unity, the oxygen concentration profile is relatively flat inside the particle whereas for effectiveness factors of the order 0.1, O_2 concentration gradients are quite steep near the particle periphery and O_2 concentrations are quite low near the particle center.

Assuming that there is no reaction in the boundary layer surrounding the coal-char particle, the oxygen partial pressure at the particle's outer surface can be shown to satisfy the relation [14]:

$$q_c = \frac{k_d P}{\gamma} \ln\left(\frac{1 - \gamma\ P_s / P}{1 - \gamma\ P_\infty / P}\right), \qquad \text{where} \quad k_d = \frac{\hat{M}_C\ D_{O_2}\ Sh}{\hat{R} T_m d_c\ \nu_{O_2}} \ . \tag{9a,b}$$

In the above relations, P, P_s, and P_∞ denote the total pressure and the partial pressures of oxygen at the particle surface and in the surroundings, respectively, and γ is the change in gas volume upon reaction per mole of oxygen consumed. Also, M_C is the molecular weight of carbon, $\hat{R}$ is the gas constant, T_m is the mean temperature between the char particle and the gas, and ν_{O2} is the number of moles of oxygen consumed per mole of carbon converted to CO and CO_2. In deriving Eqs. (9a,b), the approach of Frank-Kamenetskii [15] was used to account for the effects of Stefan flow, the convective flow that arises in the boundary layer surrounding the particle as a result of the change in volume upon reaction.

Assuming that char particles burn under steady-state conditions, gas and particle temperatures satisfy the following char-particle energy equation, which represents a balance between energy generated as a result of carbon oxidation and energy loss due to convection and radiation at the outer surface of the particle [14]:

$$q_c \Delta H = -\frac{Nu\ \lambda}{d_c} \frac{\kappa}{1 - e^{\kappa}} \left(T_c - T_\infty\right) + \varepsilon_c \sigma \left(T_c^4 - T_w^4\right), \quad \text{where} \quad \kappa = \frac{\gamma\ c_{p,g}\ d_c\ \nu_{O_2}\ q_c}{\hat{M}_C\ \lambda\ Nu} \tag{10a,b}$$

Temperature-dependent properties in the particle's boundary layer are evaluated at the mean of the gas and particle temperatures. The values of ν_{o2}, γ, and ΔH depend upon the products of the heterogeneous carbon oxidation reaction. For specified char-particle properties (d_c, ρ_c, and $S_{g,c}$), Eqs. (8) to (10a,b) permit the evaluation of q_c, P_s, and T_c, given the properties of the surrounding gas and parameters that describe the intrinsic chemical reactivity of the char.

It is assumed that the pyrite particles inside a coal-char particle (*i.e.*, the pyrite inclusions) are distributed uniformly within the carbonaceous matrix. Due to the oxygen concentration gradient inside the char particle, all the pyrite inclusions are not subjected to the same oxidation conditions. Pyrite particles closest to the periphery of the char particle experience a higher oxygen level than those near the particle center. To account for this, the char-particle effectiveness factor is used to determine an effective value of the oxygen concentration for evaluation of the oxidation rate of the pyrite inclusions. For char particles burning under typical pulverized coal combustion conditions, char-particle effectiveness factors are less than unity, and can be calculated from the particle Thiele modulus [16]. In the approach taken, $[O_2]_{eff} = \eta P_s / R T_c$, where, as already noted, P_s is the oxygen partial pressure at the outer surface of the coal-char particle, which is determined using Eqs. (8) to (10a,b). This approach is consistent with Jorgensen's [5] observation that carbon matrix effects retard pyrite oxidation. The carbon matrix presents a transport barrier to oxygen.

Thus, for pyrite inclusions in coal-char, the composition of the pyrite particle during oxidation is followed by integrating the set of mass action equations represented by Eq. (1) for all species except oxygen, for which Eq. (7a) is used with $[O_2]_\infty$ replaced by $[O_2]_{eff}$. The temperature of the pyrite inclusion is followed by integrating Eq. (2) with T_∞ and T_w replaced by T_c, the temperature of the char particle.

A computer code is under development [10] to provide predictive capabilities with respect to pyrite composition and temperature during combustion of extraneous pyrite particles or pyrite inclusions in pulverized coal. The code will implement the numerical procedure to integrate the set of differential equations (represented by Eqs. (1), (2) and (7a)) that govern pyrite oxidation during pulverized coal combustion. Reaction rate coefficients are being determined [10] that yield calculated species concentrations that agree with the measurements obtained in the pyrite combustion tests performed during the course of this project. These coefficients will be reported in upcoming publications based on the results of this work.

Conclusions

The X-ray diffraction analyses and WDS measurements indicate that the oxidation pathway of pyrite to magnetite is consistent with the reaction sequence :

$$FeS_2 \rightarrow FeS \rightarrow FeO \rightarrow Fe_3O_4 \ .$$

The size distribution measurements indicate insignificant particle fragmentation during the transformation process. At low oxidation rates, pyrite transforms to magnetite by passing through a well-defined sequence: from pyrite to troilite, to wusite, to magnetite. In 1 mol-1% oxygen at 1550 K, the conversion reaches 86 wt-% in 146 ms. At high oxidation rates, the troilite-to-wusite and the wusite-to-magnetite transformation steps can be so rapid that no troilite or wusite may be detected at early residence times. In 12 mol-% oxygen at 1550 K, 89 wt-% conversion is attained in 25 ms. The pyrite oxidation mechanism put forth is capable of predicting the salient features observed during the oxidation of pyrite under conditions pertinent to pulverized coal combustion.

The microprobe analyses of oxidized pyrite particles indicated that intraparticle mass transport resistances are negligible. Particles can be modeled as being well stirred, having insignificant compositional gradients on the scale of the particle radius. The negligible radial gradients in oxygen concentration suggests that chemical kinetics, not mass transport, is the rate-limiting intraparticle process during pyrite oxidation.

During the oxidation of an extraneous pyrite particle, the oxygen concentration at the outer surface of the particle depends on the diffusive transport of oxygen across the boundary layer surrounding the particle and on the overall pyrite reaction rate. Gas phase mass transfer and intraparticle chemical kinetics control the overall transformation rate of extraneous pyrite particles. A model for predicting the transformation rate of extraneous pyrite particles to magnetite was developed that is based on the species and energy conservation equations. The pyrite oxidation mechanism employed permits the prediction of the composition of an extraneous pyrite particle during its transformation to magnetite. The model permits the prediction of sulfur release rates during the oxidation of extraneous pyrite particles in conditions typical of those existing in pulverized coal-fired boilers and furnaces.

The oxidation rates of pyrite inclusions in coal chars depend upon char reactivity and the char-particle effectiveness factor. Carbon matrix mass transfer and chemical kinetics as well as pyrite intraparticle chemical kinetics control the overall transformation rates of pyrite inclusions. A model for the oxidation of included pyrite particles was presented that employs the use of an effective char-particle oxygen concentration when evaluating the rates of the reactions in the pyrite oxidation mechanism. The model permits the prediction of sulfur release rates during the oxidation of pyrite inclusions during pulverized coal combustion.

The time-resolved pyrite oxidation tests performed during the course of this project suggest that pyrite transforms according to a pathway that is generally similar to previously proposed transformation sequences. Nevertheless, some observations constitute notable departures from the prevailing views on pyrite combustion. These observations are noted below.

New Observations

- FeS formation during FeS_2 decomposition

  The quantitative XRD analysis of partially oxidized pyrite ash recovered from the entrained flow reactor during the course of this project showed that in 1 mol-% oxygen at 1550 K, nearly stoichiometric FeS, not $Fe_{0.875}S$, was the pyrite decomposition product after an initial point. After approximately 42 ms of residence time, FeS became the dominant sulfide. In a previous pyrite oxidation study [8], tests performed in a radiant reactor containing 6 mol-% oxygen at about 900 K (and higher) showed that after approximately 189 ms residence time, FeS became the dominant sulfide. Consequently, pyrite decomposition may not be heat transfer limited (beyond an initial heat up phase) as depicted in published pyrite combustion models. Pyrite decomposition is chemical kinetics controlled.

- Fe_3O_4 and FeO formation during FeS_2 decomposition

  In the 12 mol-% oxygen entrained flow reactor study, Fe_3O_4 was detected at all times, including the pyrite decomposition stage (even with large quantities of undecomposed FeS_2), and in the 1 mol-% oxygen study, FeO was detected as FeS_2 was decomposing. If FeS_2, FeS, and Fe_3O_4 coexist in the same particles, Fe_3O_4 formation suggests that pyrite decomposition to FeS is not externally heat transfer limited as portrayed in most published models, because Fe_3O_4 formation

from either FeS_2 or FeS is an exothermic process. Similarly, FeO formation is exothermic from either FeS_2 (if SO is assumed to be the FeS_2 oxidation product) and FeS as the initial species.

- Sulfur release during FeS_2 decomposition

  Sulfur aerosol was recovered from combustion products of all tests in the 1% study and some tests in the 12% oxygen study. Sulfur recovery implies that contrary to what is portrayed by most published models, pyrite does not decompose as a particle-within-a sulfur diffusion flame. This conclusion, in turn, implies a need to revise the prevailing view, which is that evolved sulfur consumes all of the oxygen that would flow to a decomposing pyrite particle and supplies the heat to fuel the particle's decomposition.

- Formation of crystalline FeS, FeO, and Fe_3O_4 during oxidation

  Clearly defined crystalline FeS, FeO, and Fe_3O_4 peaks were identified on XRD patterns of entrained flow reactor combustion products. Thus the results of the entrained flow reactor studies were inconsistent with the assumption underlying most published models that a blended, amorphous oxysulfide melt phase exists as an intermediate when pyrrhotite transforms from FeS to Fe_3O_4.

With respect to strategies for slag control in staged, low-NO_x pulverized-coal combustor retrofits, pyrite oxidation rates could be accelerated by increasing the heat input to selected burners. This would increase temperatures, thereby increasing the transformation rate of highly adhesive, reduced species such as FeS and FeO to the non-adhesive, oxidized species such as Fe_3O_4 and Fe_2O_3. Since carbon matrix mass transfer and kinetics retard pyrite transformation to magnetite (by reducing the oxygen concentration in the vicinity of the pyrite particles), finer grinding of the coal feed to liberate pyrite inclusions would enhance the overall pyrite conversion process. In addition, since smaller coal-char particles would have higher effectiveness factors (and hence, higher internal oxygen levels), pyrite inclusions would have higher rates of oxidation.

Acknowledgements

The authors gratefully acknowledge the support of the United States Department of Energy for support of this work under Grant # DE-FG22-94PC94205.

References

1. Reid, W. T., "Coal Ash: Its Effect on Combustion Systems," Chemistry of Coal Utilization, Second Supplementary Volume (Ed. Martin A. Elliot), John Wiley & Sons, Inc., New York, 1981.
2. Badin, E. J., "Coal Combustion Chemistry – Correlation Aspects," Elsevier Science Publishers, Amsterdam, 1984.
3. Srinivasachar, S. and Boni, A., *Fuel,* **68**, 1989, p. 829.
4. Abbott, M. F. and Austin, L. G., *Fuel,* **61**, 1982, p. 765.
5. Jorgensen, F. R. A., *Trans Inst. Min. Metall*. Sect. C, **90**, 1981, p. 1.
6. Asaki, Z., Mori, S., Ikeda, M., and Kondo, Y., *Met. Trans. B*, **16B**, 1985, p. 627.
7. Akan-Etuk, A. and Niksa, S., Paper No. 89-82 WSS/CI Fall Mtg., Livermore, CA, October 1989.

8. Akan-Etuk, A. E. J. “Pyrite Transformations During Pyrolysis,” Unpublished Report prepared under the Supervision of Prof. S. Niksa, Mechanical Engineering Department, Stanford University, 1990.

9. Huffman, G. P., Higgins, F. E. Levasseur, A. A., Chow, O., Srinivasachar, S., and Mehta, A. K., *Fuel*, **68**, 1989, p. 486.

10. Akanetuk, A. E. J. “Rate-Limiting Mechanisms of Pyrite Oxidation to the Non-Slagging Species Magnetite” Ph.D. Thesis, Mechanical Engineering Department, Stanford University, (under preparation, August 2002).

11. Mitchell, R. E., Hurt, R. H., Baxter, L. L., and Hardesty, D. R. "Compilation of Sandia Coal Char Combustion Data and Kinetic Analyses: Milestone Report," Sandia National Laboratories Report, SAND92-8208, 1992.

12. Mitchell, R. E. and Akanetuk, A. E. J. "The Impact of Fragmentation on Char Conversion during Pulverized Coal Combustion," *Proc. Combust. Inst*. **26**:3137-3144 (1996).

13. Guy, A. B. and Hren, J. J., Elements of Physical Metallurgy, Third Edition, Addison-Wesley Publishing Company, Reading, Massachusetts, 1974.

14. Mitchell, R. E., “An Intrinsic Kinetics-Based, Particle-Population Balance Model for Char Oxidation during Pulverized Coal Combustion,” *Proc.Combust. Inst.* **28**:2261-2270 (2000).

15. Frank-Kamenetskii, D. A. Diffusion and Heat Transfer in Chemical Kinetics, Plenum Press, New York, (1969).

16. Thiele, E. W., “Relation Between Catalytic Activity and Size of Particles,” *Ind. Eng. Chem*. **31**:916-920 (1939).